Petroleum Science 22 (2025) 4910–4932

Contents lists available at ScienceDirect

Petroleum Science

journal homepage: www.keaipublishing.com/en/journals/petroleum-science

Original Paper

Mobility evaluation of continental shale oil of the Permian Fengcheng Formation in the Mahu Sag: Reservoirs characteristics, multiple influencing factors and conceptual models

Yuan-Hao Zhang [a,b], Zhen-Xue Jiang [a,*], Jia-Qi Chang [c], Zhi-Ye Gao [a,**], Bo-Lin Zhang [a,b], Zhi-Wei Wang [d], Xiao-Xue Liu [e], Li-Liang Huang [f]

[a] State Key Laboratory of Petroleum Resources and Engineering, China University of Petroleum (Beijing), Beijing, 102249, China
[b] College of Geosciences, China University of Petroleum (Beijing), Beijing, 102249, China
[c] Petroleum Exploration & Production Research Institute, SINOPEC, Beijing, 100083, China
[d] School of Resources and Safety Engineering, Chongqing University, Chongqing, 400044, China
[e] College of Earth Science and Engineering, Shandong University of Science and Technology, Qingdao, 266590, Shandong, China
[f] Research Institute of Petroleum Exploration and Development, PetroChina Xinjiang Oilfield Company, Karamay, 834000, Xinjiang, China

ARTICLE INFO

Article history:
Received 29 December 2024
Received in revised form
26 June 2025
Accepted 9 September 2025
Available online 15 September 2025

Edited by Jie Hao and Xi Zhang

Keywords:
Continental shale
Lithofacies
Shale oil mobility
NMR-centrifugation
Pore structure
Fengcheng Formation

ABSTRACT

Mobility is a crucial metric for assessing sweet spots of continental shale oil. However, due to the complexity of shale oil reservoirs characteristics and the lack of systematic analyses of factors influencing mobility, the difference in shale oil mobility under multiple lithofacies control remains unclear, causing significant challenges for mobility evaluation and sweet spot prediction. This study examines continental shales of the Fengcheng Formation in the Mahu Sag, employing scanning electron microscopy (SEM), nitrogen adsorption (NA), nuclear magnetic resonance (NMR), spontaneous imbibition (SI), and contact angle measurements (CAM) to investigate the pore structure, connectivity, and wettability properties of different lithofacies shale. Quantitative analyses of shale movable oil content and saturation were conducted using multistep temperature pyrolysis (MTP) and NMR centrifugation techniques. Furthermore, the influence of reservoir characteristics, geochemical characteristics, and lamination development on shale oil mobility were discussed. Results indicate that larger pore diameter, higher imbibition slopes, and lower fractal dimensions of movable fluid pores (D_2) correspond to higher movable oil saturation. Organic matter exerts a dual effect on shale movable oil content. When the TOC is below a threshold, the movable oil content gradually increases with TOC. Laminations exhibit favorable reservoir properties and light oil enrichment, enhancing shale oil mobility. Massive siltstone (MS) develops interconnected intergranular pores with the best pore structure and connectivity, the lowest D_2 values, and the highest shale oil mobility. Laminated felsic shale (LFS) and laminated calcareous shale (LCS) exhibit moderate mobility, where the development of microfractures enhances fluid flow by connecting isolated pores into pore-fracture networks. In contrast, massive felsic shale (MFS) and bedded felsic shale (BFS) primarily develop intragranular dissolution pores with more complex structures and poorer connectivity, resulting in weaker mobility. A more accurate approach for assessing shale oil mobility has been presented, taking into account both total oil content and movable oil saturation. More importantly, this study establishes a comprehensive conceptual model illustrating the potential relationships among shale lithofacies, reservoir characteristics, and movable oil flow space in the study area. This research not only provides a systematic approach for assessing shale oil mobility but also deepens the understanding of flow mechanisms of continental shale oil, offering theoretical guidance for optimizing sweet spots in the Fengcheng Formation shale oil reservoirs of the Mahu Sag.

* Corresponding author.
** Corresponding author.
E-mail addresses: jiangzx@cup.edu.cn (Z.-X. Jiang), gaozhiye@cup.edu.cn (Z.-Y. Gao).
Peer review under the responsibility of China University of Petroleum (Beijing).

https://doi.org/10.1016/j.petsci.2025.09.019

1. Introduction

As conventional petroleum resources become depleted, oil contained within low-porosity and ultra-low-permeability shale formations is considered a highly promising unconventional resource (Slatt, 2011; Arthur and Cole, 2014; Zou et al., 2019). Over the past decade, the shale oil and gas revolution in North America has profoundly reshaped the world's energy supply framework (Curiale and Curtis, 2016; McMahon et al., 2024). Against this backdrop, China has progressively enhanced its exploration of shale oil resources, achieving significant progress in multiple basins (Wang et al., 2019a; Fu et al., 2020; Sun et al., 2021). Unlike North America's marine shale oil, China's shale oil primarily develops within continental strata, which are marked by complex lithofacies, strong reservoir heterogeneity, higher oil viscosity and poor mobility (Hu et al., 2020; Jin et al., 2021b). These characteristics not only result in low recovery rates, but also lead to rapid production decline of wells, further increasing the difficulty of the exploration and development of continental shale oil. Notably, the production value of shale oil depends on the quantity of movable oil within reservoirs, with mobility directly determining extraction efficiency and well productivity (Jin et al., 2021a; Zhao et al., 2021). Therefore, in order to efficiently explore and utilize unconventional resources, evaluating shale oil mobility becomes a crucial scientific issue.

Currently, the evaluation of shale oil mobility primarily focuses on two aspects: geochemistry and reservoir pore structure. Commonly employed methods include multi-solvent extraction, multistep temperature pyrolysis (MTP), oil saturation index (OSI, $100 \times S_1$/TOC), molecular dynamics simulations, nuclear magnetic resonance (NMR) and centrifugation (Jiang et al., 2016; Wang et al., 2016; Piedrahita and Aguilera, 2017; Li et al., 2019c; Zhu et al., 2021; Tian et al., 2024). Among them, multi-solvent extraction and MTP determine the movable oil content (light hydrocarbons and medium hydrocarbons) in fresh powdered sample through polar solvent extraction or graded heating experiments. However, these processes destroy the original pore structure of shale. The OSI technique classifies and assesses shale oil resources, asserting that only enriched shale oil resources exhibit fluidity (Gong et al., 2021). Here, movable oil refers to hydrocarbons that are expelled after overcoming the adsorption retention capacity of organic matter. Generally, higher OSI values indicate better mobility. However, this method also ignores the physical limitations of the pore system. Molecular dynamics method models the adsorption and free movement of hydrocarbons in nanopores, offering insights into the flow mechanisms of shale oil in pores ranging from a few nanometers to tens of nanometers (Tian et al., 2018; Song et al., 2024). Nonetheless, the simulated pore sizes are limited, and the models are overly theoretical, failing to characterize shale oil mobility in the actual core reservoir space. NMR combined with centrifugation is frequently used to evaluate fluid mobility in actual shale reservoir spaces (Karimi et al., 2015; Zhu et al., 2021; Pang et al., 2022; Zhang et al., 2022). That is, the fluid mobility in different scale pore sizes is quantitatively characterized by the NMR T_2 spectrum before and after centrifugation. Additionally, in fluid-saturated shale, the NMR T_2 cutoff (T_{2c}) value distinguishes between bound fluids (immobile) and free fluids (movable oil or water) (Testamanti and Rezaee, 2017; Liu et al., 2018). The NMR fractal dimension for signals exceeding the T_{2c} value can indicate the heterogeneity of the pore containing movable fluids (Zhang and Hu, 2020; Zang et al., 2022). The results obtained from these methods often differ significantly. To address the limitations of single approach, the evaluation of shale oil mobility must combine different methods, considering oil content and pore structure (Bai et al., 2022, 2023; Chang et al., 2024).

Shale is widely recognized for its complex reservoir characteristics, with the flow of shale oil considerably limited by numerous nanoscale pores, variable bedding structures, pore heterogeneity, and intricate flow pathways in the shale reservoir (Jiang et al., 2020; Pang et al., 2023; Cai et al., 2024; Cao et al., 2024a; Li et al., 2024a). In addition, due to the strong interfacial interactions between fluids and pore surfaces, surface wettability is another critical factor influencing mobility (Li et al., 2024c). It is essential to first describe key reservoir elements including pore structure, connectivity, and wettability in order to accurately assess shale oil mobility. From a geochemical perspective, organic matter, which governs oil retention and migration, directly impacts shale oil enrichment and, consequently, the movable oil content. However, the effect of organic matter on shale oil mobility is complex, the relationship between movable oil content and total organic carbon (TOC) may be positive (Bai et al., 2023; Zhang et al., 2023; Hu et al., 2024) or negative (Nie et al., 2024; Xiao et al., 2024), a phenomenon that remains inadequately elucidated. Formation pressure, as a driving force, is also a crucial factor affecting shale oil mobility. Increased formation pressure enhances dissolved gas concentration in shale oil, reduces adsorption capacity and viscosity, and thereby improves fluid mobility (Wang et al., 2019b). However, in a specific region or formation, pressure tends to remain uniform and can often be disregarded. Therefore, studies on the factors influencing continental shale oil mobility requires to be considered from both reservoir characteristics and organic geochemistry.

Lithofacies represent the rocks types and their spatial assemblage characteristics formed in specific sedimentary environments (Oboh-Ikuenobe et al., 2005; Princeton Dim et al., 2016; Shu et al., 2021). Due to frequent shifts in sedimentary environments, continental shale formations often exhibit diverse bedding structures and complex lithofacies combinations (Gao et al., 2018a; Liu et al., 2021). These variations in lithofacies directly result in prominent disparities in reservoir pore structure and oil-bearing properties, thereby influencing shale oil mobility (Cao et al., 2024b). For instance, in the Paleogene Kongdian Formation of the Cangdong Sag, laminated felsic shale are regarded as “sweet spot” intervals with higher mobility (Han et al., 2021). Similarly, in the mixed sedimentary sequences of the Lucaogou Formation, high-carbon micritic dolomites exhibit excellent reservoir performance and fluid mobility, making them favorable “sweet spot” layers (He et al., 2024). Thus, identifying lithofacies with the highest mobility is crucial for pinpointing “sweet spots” within complex shale formations.

Currently, shale oil in the Fengcheng Formation of the Mahu Sag, as a critical continental shale oil resource, has become focal point for exploration in China (Tang et al., 2021). Recent, wells MY1, MY1H, and MY2 in Mahu Sag have been drilled to assessed the exploration potential of Permian continental shale oil in the Fengcheng Formation. According to 2022 measurements by the Xinjiang Oilfield Company of PetroChina, well MY1 had a peak daily crude oil production of 50.6 m^3, with cumulative output exceeding 5000 m^3, highlighting significant resource potential. Concurrently, a growing number of studies have focused on the Fengcheng Formation shale oil, especially concentrating on sedimentary palaeoenvironment and geochemical characteristics (Yu et al., 2018, 2019; Zhang et al., 2018b), reservoir property evaluation (Wang et al., 2021; Du et al., 2023) and shale oil enrichment (Jiang et al., 2023; Liu et al., 2023; Jia et al., 2024). Some recent works have also preliminarily discussed shale oil mobility of Fengcheng Formation using geochemical indicators such as S_1 or OSI (Chang et al., 2022; He et al., 2022). However, systematic studies on the mobility of shale oil and its affecting factors in Fengcheng Formation remain lacking, particularly regarding

comprehensive evaluations considering reservoir pore structure, geochemical characteristics, lamination development, and lithofacies control. Moreover, most of the existing mobility evaluation methods tend to emphasize a single aspect without quantitatively coupling oil-bearing parameters with actual physical measurements such as NMR and centrifugation-based evaluation. These gaps significantly hinder the accurate identification of "sweet spots" in shale formations and the optimization of extraction strategies. In response, this study employs various laboratory experiments to evaluate the mobility of continental shale oil in the Fengcheng Formation, aiming to achieve the following objectives: (1) define the pore structure, connectivity, surface wettability, and mobility characteristics of the shale oil reservoir; (2) evaluate multiple influencing factors of shale oil mobility; (3) propose a novel method for shale oil mobility evaluation considering total oil content and movable efficiency; (4) construct a conceptual model illustrating the mobility differences among various lithofacies in the Fengcheng Formation.

2. Geological setting

The Junggar Basin is a huge continental overlying oil-bearing basins in Northwest (NW) China. With a total area of 13.4×10^4 km^2, the basin is separated into six second-order structural units, including the South Tianshan Piedmont Thrust Belt, the Central Depression, the Wulungu Depression, the Luliang Uplift, the Western Uplift, and the East Uplift (Fig. 1(a)) (Tao et al., 2019; Cao et al., 2020; Aman et al., 2023). The Mahu Sag, situated in the northwestern part of the Central Depression, is a prominent hydrocarbon-generating sags, covering an area of approximately 5000 km^2 (Zhi et al., 2019). Its western is bounded by the Wuxia and Kebai Fault Zone, while the northern boundary limit adjoins the Yingxi Sag. From the east to south, the sag is bordered by the Sangequan, Xiayan, Dabasong, and Zhongguai Uplift, with a predominant NE-SW orientation (Fig. 1(b)).

The Fengcheng Formation developed within a mixed alkaline lake depositional sequence, influenced by terrigenous detrital

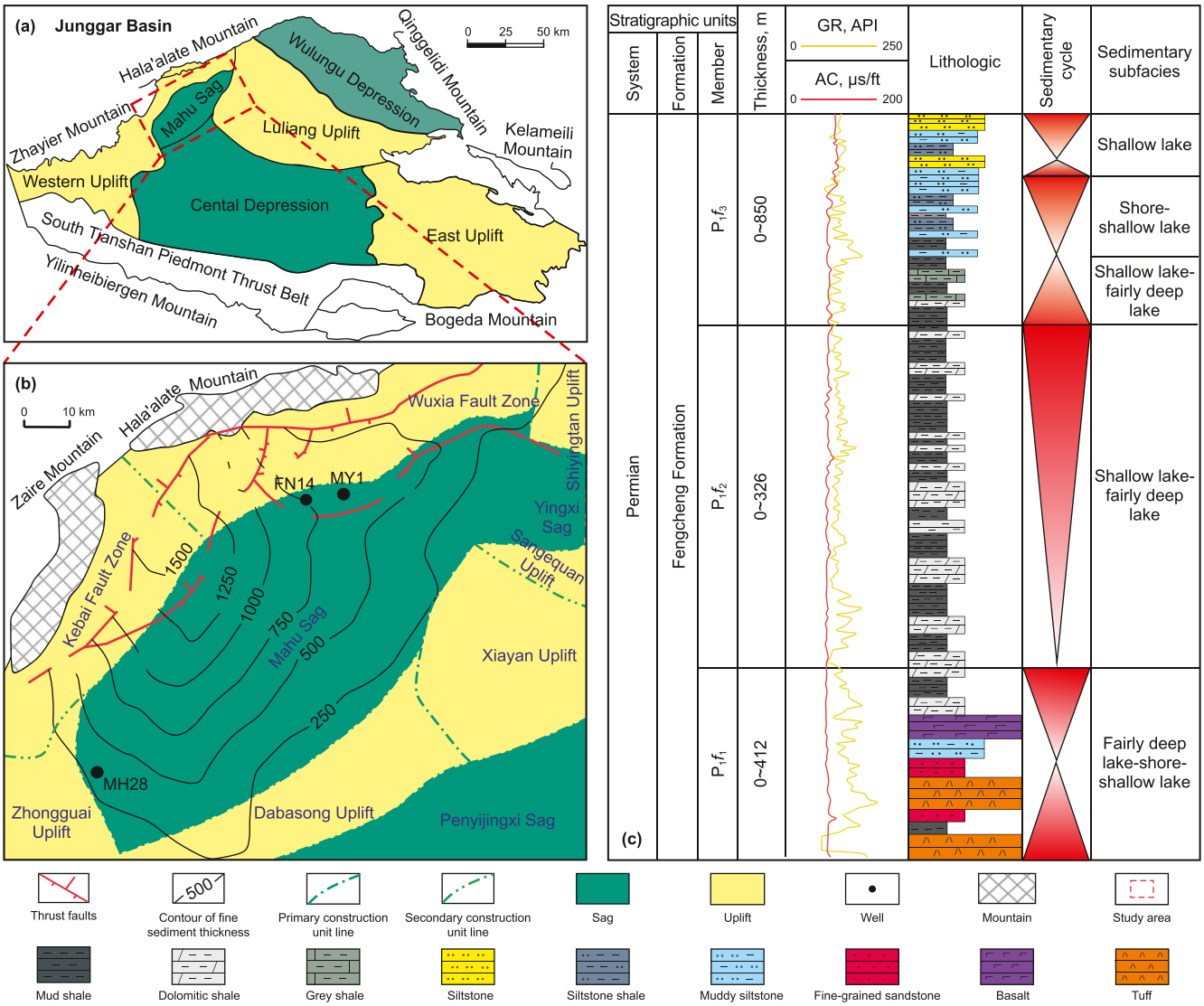

Fig. 1. **(a)** The structural map of Junggar Basin and the position of Mahu Sag. **(b)** Mahu Sag's geological structure and sample well location (modified from Zhi et al. (2021)). **(c)** Stratigraphic column of Permian Fengcheng Formation, including lithology and sedimentary cycle (modified from Wang et al. (2021); Huang et al. (2022)).

influx, volcanic activity, and hydrothermal processes (Tang et al., 2020; Guo et al., 2021). Owing to variations of lacustrine basin water conditions and sedimentary cycles, this formation can be separated into three members: Feng 1 Member (P_1f_1), Feng 2 Member (P_1f_2), and Feng 3 Member (P_1f_3) (Fig. 1(c)) (Zhi et al., 2021). The P_1f_1 represents a lake transgressive deposit sequence characterized by frequent volcanic activity, with tuffaceous and volcanic rocks at the base transitioning into mudstones and dolomitic shales at the top (Yu et al., 2019; Wu et al., 2022). The P_1f_2 corresponds to a highstand deposit sequence, marked by the strongest evaporation, highest salinity, and the development of alkaline minerals. Its lithology is mostly composed of organic-rich mud shales and dolomitic shales (Xia et al., 2020; Guo et al., 2021; Du et al., 2023). The P_1f_3 represents a lake regressive deposit sequence, with mudstones and calcareous shales in the lower part transitioning to fine-grained clastic rocks at the top due to increased terrigenous clastic material (Tang et al., 2021; Huang et al., 2023).

3. Samples and experimental methods

3.1. Samples

This investigation selected 16 core samples from the wells MY1, FN14, and MH28, with coring depths between 4075.60 and 4933.50 m. Samples MY-1 to MY-4 were taken from well FN14, MY-5 to MY-14 from well MY1, and MY-15 and MY-16 from well MH28. Each sample was collected along the bedding plane, comprising shale and siltstone from interbeds. The fresh samples were divided into four parts for experimental analysis, as illustrated in Fig. 2. First, cylindrical plugs (length:diameter = 5 cm:2.5 cm) were extracted for porosity, permeability and NMR experiments. The second part was ground into powdered samples for X-ray diffraction (XRD), TOC, MTP, and nitrogen adsorption (NA) experiments. The third part was cut into cubic samples of 1 cm^3 for spontaneous imbibition (SI) tests with oil and water, as well as contact angle measurements (CAM). The remaining portions were used to prepare thin sections (TS) and conduct field emission scanning electron microscopy (FE-SEM) observations.

3.2. Experimental methods

3.2.1. TOC, XRD, NA and MTP analysis

After pulverizing and sieving the all samples to 200 mesh, mineral composition and TOC analyses were conducted using a Rigaku Miniflex II X-ray diffractometer and a LECO CS230HC carbon-sulfur analyzer, respectively. The XRD measurement process adhered strictly to the Chinese Oil and Gas Industry Standard SY/T5163-2010. In the TOC treatment procedure, the shales were first immersed in hydrochloric acid solution at a concentration of 12.5% for two days to remove inorganic carbon. Subsequently, after 12 h of drying in the 80 °C incubator, TOC content was determined using infrared detector.

Prior to the NA tests, all shales were oil-washed and pulverized to 80 mesh. The processed samples were then analyzed using the Micromeritics ASAP 2460 instrument. The experiment employed high-purity nitrogen gas as the adsorbate and was conducted at cryogenic temperatures (−196 °C) under a pressure range of 97.3 to 27.0 kPa.

Shale samples were crushed to 100 mesh and analyzed using Rock Eval 7 pyrolysis apparatus for MTP experiments. The detailed experimental procedure is referred to Chang et al. (2024). Upon completion, hydrocarbons generated at different temperature stages were analyzed using pyrolysis chromatography: $S_{1\text{-}1}$ shows light hydrocarbons fractions, $S_{1\text{-}2}$ corresponds to light and medium hydrocarbons released during heating, $S_{2\text{-}1}$ indicates heavy hydrocarbons, resins, and asphaltenes, and $S_{2\text{-}2}$ reflects hydrocarbons derived from kerogen pyrolysis (Jiang et al., 2016). In this analysis,

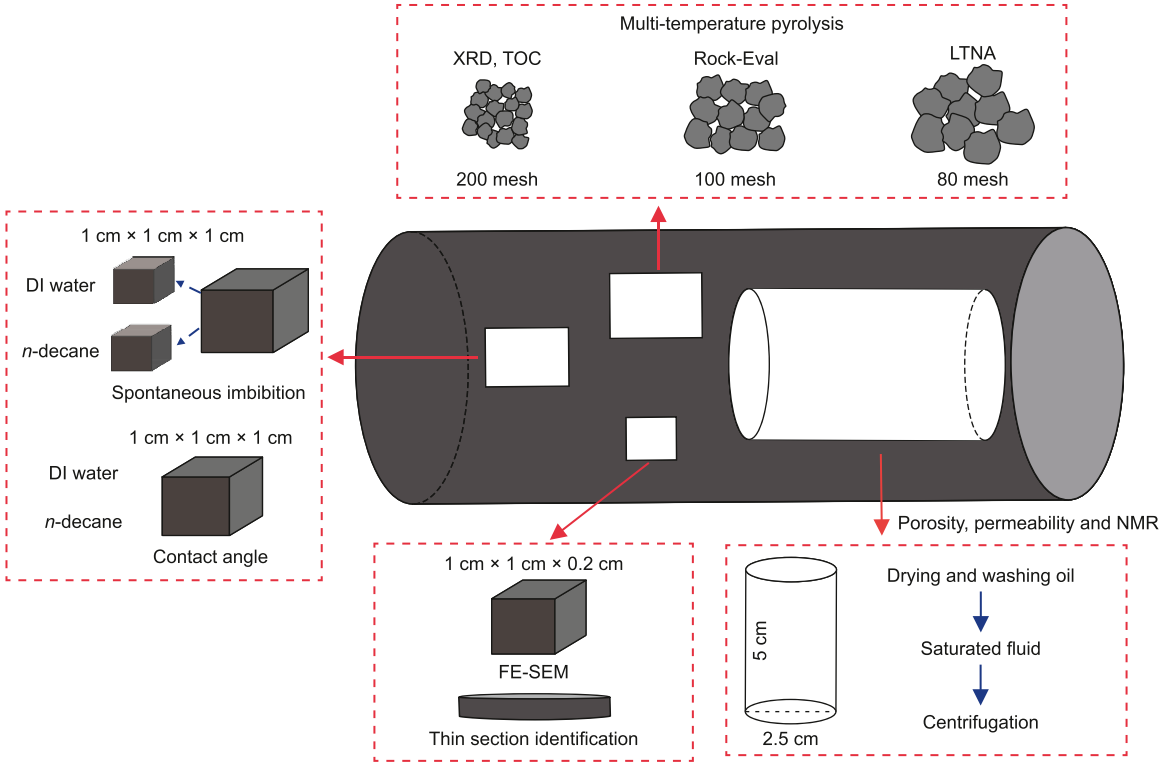

Fig. 2. Flowchart of experimental sample processing in Fengcheng Formation.

$S_{1\text{-}1}+S_{1\text{-}2}$ signifies the maximum movable oil content, $S_{2\text{-}1}+S_{2\text{-}2}$ corresponds to the adsorbed oil content, and $S_{1\text{-}1}+S_{1\text{-}2}+S_{2\text{-}1}+S_{2\text{-}2}$ denotes the total oil content.

3.2.2. Porosity and permeability experiments

After oil washing and drying the cylindrical plugs samples, an AP-608 automated overburden porosity and permeability testing system was employed according to GB/T 34533-2023. A helium gas injection pressure of 6.895 MPa was applied to measure the porosity and permeability of all samples. The tests were conducted under standard humidity (21–24 °C) and temperature conditions (10%–20%).

3.2.3. TS and FE-SEM observation

The bedding structures and mineral optical properties of rocks were identified through thin section observation. Samples were repeatedly ground until reaching a thickness of 0.02–0.06 mm, followed by examination using an OLYMPUS BX3M-LEDR optical microscope at varying magnifications. Each sample were captured under polarized light of two different directions. The focus travel range was 25 mm, with each fine adjustment increment measuring 100 μm.

Before FE-SEM observation, each sample was prepared into a cubic shape with dimensions of approximately 1 cm × 1 cm × 0.2 cm. The samples underwent polishing through argon ion cross-sectioning process, followed by the application of carbon film to enhance conductivity. Observations were conducted by ZEISS Merlin SEM operating at a beam current of 15 kV.

3.2.4. SI and CAM

SI experiments refers to the process by which fluids are driven into pores under the influence of capillary forces (Geistlinger and Mohammadian, 2015; Gao et al., 2018b). The shales were chopped into 1 cm^3 cubes for SI experiments. To prevent fluid evaporation, epoxy resin was applied to four sides of each sample, leaving only two surfaces (top and bottom) exposed. Before the experiment, the samples were dried in the 60 °C incubator for 48 h. SI experiments were conducted using two fluids: DI water and oil (*n*-decane). The imbibition mass was measured using a Shimadzu AUW220D balance with a resolution of 0.00001 g. During the experiment, the sample's bottom surface was immersed approximately 1 mm into the imbibition fluid. To maintain constant humidity, four small beakers filled with DI water were placed in the test box, following the approach outlined by Gao and Hu (2016). All SI tests were conducted parallel to the bedding planes.

The CAM was measured using JY-82 video optical contact angle meter. Shale samples were first sectioned into 1 cm^3 cubes. To minimize the influence of surface roughness on the experiment, the testing surface was polished using 2000-mesh sandpaper. Subsequently, the samples were dried in a 60 °C incubator for 24 h. Deionized water and *n*-decane, with a droplet size of 2 μm, were used as probe liquids. The wettability contact angles of the air-water-rock and air-oil-rock surfaces were measured. Each contact angle was obtained from a single measurement, and the spreading process of a droplet was recorded using the computer-controlled camera to ensure accuracy.

3.2.5. NMR and centrifugation

The NMR technology is to detect the resonance frequency of the H nucleus in a porous medium by applying a radiofrequency magnetic field. NMR measurement of saturated shale can obtain fluid signals and pore distribution within reservoir space. Both diffuse and bulk relaxation may be disregarded under a homogenous magnetic field (Mitchell et al., 2010; Daigle and Johnson, 2016). Thus, the transverse relaxation time T_2 may be expressed as:

$$\frac{1}{T_2}=\rho_2\frac{S}{V}=\rho_2\frac{F_s}{d} \tag{1}$$

where T_2 denotes the transverse relaxation time, ms; ρ_2 is the surface relaxivity, μm/ms; S represents the total pore surface area, cm^2; V is the volume of pores, cm^3; F_s represents the pore shape factor, for spherical pores, F_s is 3, while for cylindrical pores, F_s is 2; d is the pore diameter (PD), nm.

Assuming $C=\rho_2F_s$, Eq. (1) can be reformulated as:

$$d=\rho_2F_sT_2=CT_2 \tag{2}$$

According to Eq. (2), a linear relationship exists between the T_2 and PD, allowing pore size to be calculated from the T_2 spectrum. However, due to the absence of detailed information regarding spin-electron interactions on the rock surface, the ρ_2 cannot be directly obtained and must instead be estimated using indirect methods (Saidian and Prasad, 2015; Washburn et al., 2017; Zheng et al., 2019). In this research, the ρ_2 was obtained by fitting the pore size distribution (PSD) of nitrogen adsorption data and the frequency distribution of NMR signals, and then convert the T_2 spectrum into PSD curves. The details can be referred to Li et al. (2019a).

By incorporating the adsorption ratio equation, the NMR distribution characteristics of adsorbed and free oil can be quantitatively characterized (Li et al., 2018a; Li et al., 2019b). Free oil consists of movable oil and capillary-bound oil (Zang et al., 2022). The adsorption ratio Eq. (3) is expressed as follows:

$$r_a=\frac{1}{1+\frac{\rho_f}{\rho_a}\left(\frac{d}{F_sH}-1\right)} \tag{3}$$

where r_a represents the proportion of adsorbed oil, ρ_a and ρ_f are the densities of adsorbed oil and free oil, respectively, H denotes the adsorption thickness.

Furthermore, based on the NMR T_2 spectrum and the aforementioned equation, the adsorption ratio corresponding to each T_2 value in the T_2 spectrum can be obtained:

$$r_{ai}=\frac{1}{1+\frac{\rho_f}{\rho_a}\left(\frac{T_{2i}\rho_2}{H}-1\right)} \tag{4}$$

where T_{2i} represents the ith T_2 value in the NMR T_2 spectrum; r_{ai} denotes the adsorption ratio fraction corresponding to T_{2i}.

A MicroMR series nuclear magnetic resonance core analyzer, operating at a magnetic field intensity of 0.5 ± 0.03 T and a resonance frequency of 12 MHz, was employed for this experiment. During testing, the magnetic field temperature was maintained at 32 ± 0.1 °C, with a waiting time of 3000 ms, an echo number of 17500, and an echo interval of 0.1 ms.

The centrifugation experiment can evaluate the capacity of shale oil to overcome pore capillary forces and flow out of the pore space under centrifugal force. Fluids retained after centrifugation are referred to as bound fluids, while those that can freely flow out are termed movable fluids. The experiment was conducted using an HC-3018R low-temperature high-speed centrifuge. The low temperature minimizes experimental errors caused by oil volatilization, and higher centrifuge speeds correspond to greater centrifugal forces. The magnitude of the centrifugal force can be calculated based on the centrifuge speed, the outer rotational

radius, and the density difference between the two-phase fluids (Karimi et al., 2015).

The following is the specific experimental protocol: (1) Place the standard core plug sample in the oil washing solvent (dichloromethane:methanol = 93:7) for a week to eliminate remaining oil (Ram et al., 2022; Wang et al., 2024). Then dry it in a 105 °C oven for 24 h to eliminate any remaining water. Measure the T_2 spectrum of the dried sample using an NMR analyzer and record the sample's weight and volume. (2) Subject all sample to vacuum treatment at −0.1 MPa for 2 h, and then saturate it with anhydrous paraffin at 25 MPa for 48 h. Record the T_2 spectrum after saturation and the corresponding weight. (3) Place the sample in the high-speed centrifuge set to a temperature of 10 °C. Centrifuge at 11,000 rpm for 8 h, which corresponds to a centrifugal force of 2.75 MPa. After centrifugation, record the T_2 spectrum and weight of the sample. The selected speed (11000 rpm) not only balances maximizing fluid extraction and sample integrity, but is also a widely used centrifugation condition for evaluating fluid mobility in shale and tight reservoirs, as many previous studies have done (Zheng et al., 2023; Li et al., 2024b; Wang et al., 2024).

The signal area under the NMR T_2 spectrum corresponds to the fluid volume within the pores, with larger areas indicating higher oil volumes. By integrating the signals from the T_2 spectra of the saturated and centrifuged states and subtracting them, the signal area corresponding to movable oil can be obtained. The movable oil signal area is then divided by the T_2 signal area from the saturated state (excluding the dried state T_2 spectrum signal area) to calculate the movable oil saturation during centrifugation. By integrating the NMR signal areas across different pore size ranges before and after centrifugation, the movable oil saturation in various pore scales can be determined. The specific calculation formula is as follows:

$$S_m = 1 - S_b = \frac{S_o - S_c}{S_o - S_d} = \frac{\int_{T_{2\,min}}^{T_{2\,max}} T_{Fo} dT_2 - \int_{T_{2\,min}}^{T_{2\,max}} T_c dT_2}{\int_{T_{2\,min}}^{T_{2\,max}} T_{Fo} dT_2 - \int_{T_{2\,min}}^{T_{2\,max}} T_d dT_2} \quad (5)$$

where S_m and S_b are the movable and bound oil saturation, %; S_o, S_c and S_d are the areas of T_2 spectra for the saturated, centrifuged, and dried states, respectively; T_{2max} and T_{2min} are the maximum and minimum transverse relaxation times, ms; T_{Fo}, T_c and T_d are the T_2 response amplitudes recorded in the fully saturated, centrifuged, and dried states, respectively.

3.2.6. NMR PSD and fractal theory

NMR can provide a more accurate representation of the multiscale PSD characteristics of shale (Li et al., 2018b). To accurately reflect the fluid distribution within the shale's actual pore spaces and avoid overestimating the proportion of small pores, it is necessary to subtract the NMR signal of the dry state shale from the fully oil-saturated state shale (Zhao et al., 2022). Utilizing the pore classification method commonly used in shale oil reservoirs, pores were categorized as micropores (<100 nm), mesopores (100–1000 nm), and macropores (>1000 nm) (Zhang et al., 2018a, 2025).

The fractal dimension (D) is a quantitative indicator for evaluating pore heterogeneity and structural complexity (Pfeifer and Avnir, 1984; Chandra et al., 2022). Typically ranging from 2 to 3, the value nearer to 3 signifies greater surface roughness, more intricate pore structures, and heightened heterogeneity. In recent years, NMR fractal models have been extensively used to characterize the intricacy of shale pore structures (Zhou and Kang, 2016; Yuan and Rezaee, 2019). The fractal dimension of shale is calculated using the below equation:

$$\lg(V) = (3 - D)\lg(T_2) + (D - 3)\lg(T_{2max}) \quad (6)$$

where V represents the proportion of cumulative PV with transverse relaxation time less than T_2.

A linear correlation between Lg(V) and Lg(T_2) confirms that shale pores have self-similarity and fractal characteristics. The regression analysis's slope may then be used to determine the D.

By applying the T_{2c} value, the pore spaces of movable and bound fluids may be distinguished, segmenting the curve into two regions. Subsequently, two fractal trend lines are obtained by fitting the two curves, which correspond to the fractal dimension D_1 of bound fluid pore space and the fractal dimension D_2 of movable fluid pore space in shale. The method of obtaining the T_{2c} value is shown in Fig. 3. First, the NMR signals of the oil-saturated and centrifuged states are converted into cumulative curves. A horizontal line is then drawn at the maximum cumulative signal of bound-fluid, and its intersection with the cumulative signal of the saturated state is identified. From this intersection, a vertical line is extended to the T_2 axis, defining the T_{2c} value.

4. Result

4.1. TOC, mineral composition and lithofacies characteristics

As shown in Table 1, the TOC content of shale in the study area varies from 0.106% to 1.819%, with a mean of 0.709%. The inorganic mineral content of shale mostly comprises felsic minerals (quartz and feldspar) and carbonate minerals (dolomite and calcite). The mean proportion of felsic minerals is 53.1% (range from 32.4% to 81.8%). Specifically, the mean proportion of quartz is 28.7% (range from 12.8% to 72.3%), and the mean proportion of feldspar is 24.4% (range from 9.5% to 44.8%). The mean proportion of carbonate mineral proportion is 34.1% (range from 12.1% to 60.4%) with a mean of 24.8% for dolomite and 9.9% for calcite. In contrast, the clay mineral content in the study area is minimal, not exceeding 8.8%. Additionally, a certain amount of pyrite is developed within the shales, with a mean proportion of 7.6% (ranging from 2.3% to 15%).

Interbedded sandstone and shale deposits are commonly observed in continental shale formations, and the Fengcheng Formation is no exception, featuring extensive siltstone interbeds (Gong et al., 2023; Wang et al., 2023). In this research, siltstone and shale were distinguished according to grain size, with siltstone defined by mineral grains exceeding 62.5 μm. Observations from cores and TS reveal that horizontal bedding is prominently

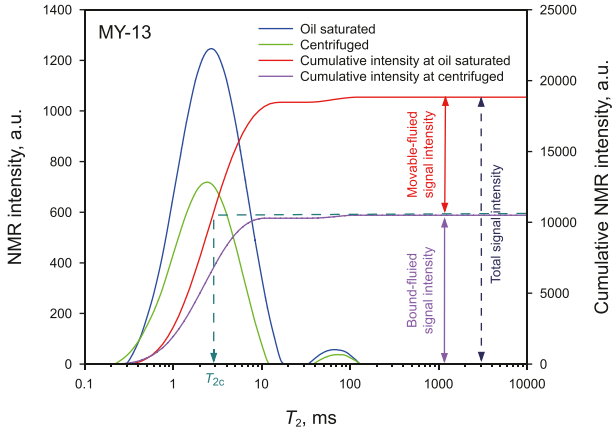

Fig. 3. Calculation of T_{2c} value in NMR and centrifugation experiments.

Table 1
TOC, inorganic mineral content, porosity and permeability parameters of samples (Partial data from Chang et al. (2024)).

Sample	Depth, m	Lithofacies	Mineral composition, wt%							TOC, %	Porosity, %	Permeability, 10^{-6} μm^2
			Q	F	Ca	D	P	Cl	O			
MY-1	4075.60	BFS	60.6	13.2	0.7	13.8	4.3	7.4	N/A	1.212	1.98	2.283
MY-2	4105.80	LCS	17.5	15.6	2.8	56.1	2.3	4.4	1.3	0.464	0.18	0.818
MY-3	4166.05	LCS	12.8	18.8	20.6	39.8	5.7	N/A	2.3	1.819	2.11	0.579
MY-4	4167.90	BFS	15.9	31.6	3.7	35.7	7.2	3.6	2.3	0.843	0.78	1.124
MY-5	4582.60	MFS	28.8	25.0	25.6	4.7	9.6	6.3	N/A	0.106	2.21	0.128
MY-6	4592.92	LFS	59.3	8.6	4.2	17.2	10.7	N/A	N/A	0.876	2.31	2.515
MY-7	4594.36	LCS	19.6	14.9	N/A	50.9	7.0	1.9	5.7	0.378	1.61	4.388
MY-8	4749.45	LCS	17.2	15.2	29.3	28.1	8.9	N/A	1.3	0.656	1.41	0.742
MY-9	4759.47	LFS	13.8	44.0	2.2	29.8	10.2	N/A	N/A	0.819	1.79	1.804
MY-10	4787.65	LFS	72.3	9.5	5.6	6.5	4.9	N/A	1.2	0.821	1.61	1.983
MY-11	4820.55	BFS	20.9	29.9	N/A	41.0	7.1	1.1	N/A	0.415	1.89	0.096
MY-12	4829.15	MFS	35.4	25.8	N/A	27.2	6.2	3.9	1.5	0.581	0.45	0.428
MY-13	4848.60	MS	14.2	35.4	10.0	22.8	15.0	N/A	2.6	0.725	10.62	21.731
MY-14	4858.41	LFS	36.2	19.2	21.3	9.8	8.4	5.1	N/A	0.672	3.42	17.968
MY-15	4931.15	MS	14.4	44.8	14.7	3.3	5.8	5.2	11.8	0.480	4.33	15.503
MY-16	4933.50	BFS	20.1	38.4	8.0	9.8	8.7	8.8	6.2	0.484	0.45	0.821

Note: Q—quartz; F—feldspar; Ca—calcite; D—dolomite; P—pyrite; Cl—clay; O—others; N/A—not available.

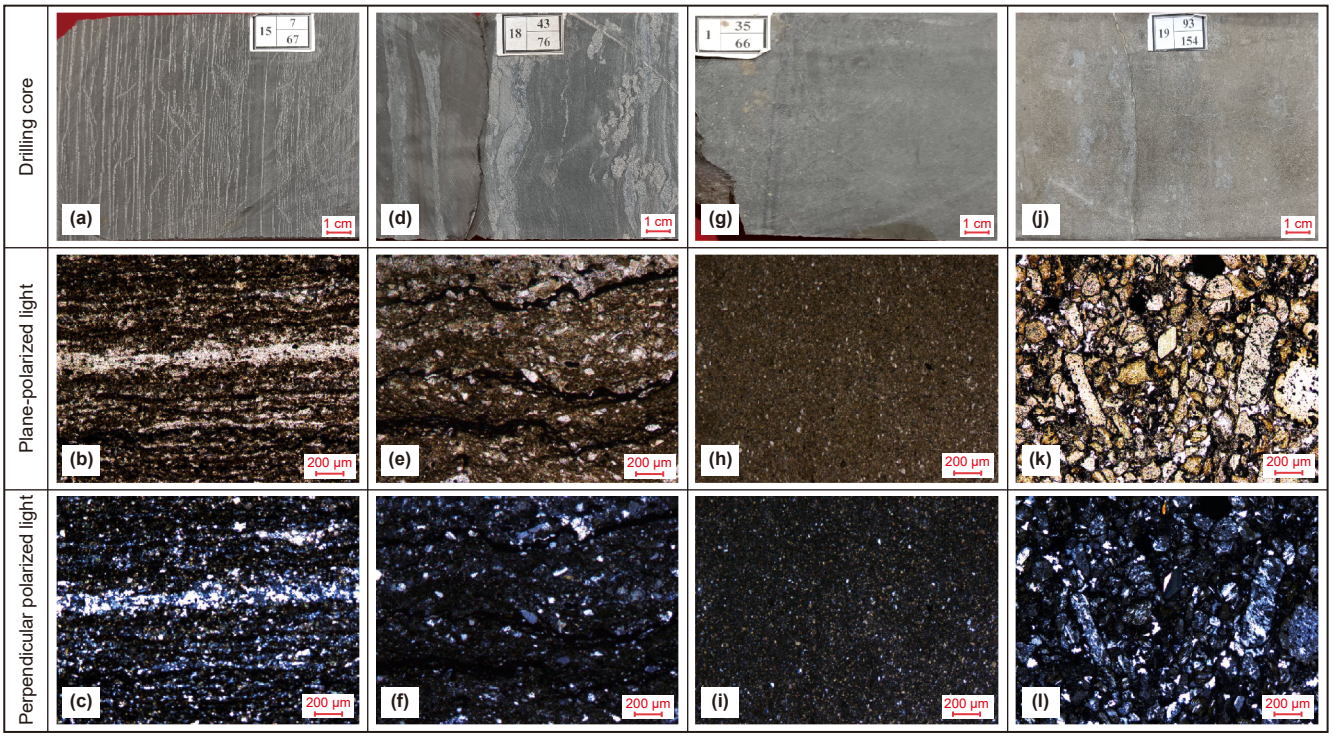

Fig. 4. Primary sedimentary structures types developed in the shale strata of the Fengcheng Formation. **(a–c)** Laminated shale, MY-10. **(d–f)** Bedded shale, MY-11. **(g–i)** Massive shale, MY-5. **(j–l)** Massive siltstone, MY-13.

developed in the Fengcheng Formation shale (Fig. 4(a)–(c)). Based on bedding thickness, three structures were identified: laminated structures (<1 mm), bedded structures (>1 mm), and massive structures (Gao et al., 2018a). In laminated and bedded structures, mineral particles are arranged in banded distributions with pronounced orientation (Fig. 4(b), (c), (e) and (f)), whereas in massive structures, minerals are evenly distributed without directional alignment (Fig. 4(h) and (i)). In contrast, the siltstone samples exhibit larger mineral grains size and more obvious pore space (Fig. 4(j)–(l)). The mineral ternary diagram shows that shale samples primarily fall into siliceous (felsic minerals >50%) and calcareous (calcareous minerals >50%) lithofacies groups (Fig. 5). Accordingly, the Fengcheng Formation rock samples were classified into five lithofacies types based on grain size, bedding structure and mineral composition: massive siltstone (MS), laminated felsic shale (LFS), laminated calcareous shale (LCS), bedded felsic shale (BFS), and massive felsic shale (MFS).

4.2. Microscopic pore structure characteristics

4.2.1. Pore type

Based on FE-SEM observations, various pore types have been identified in the Fengcheng Formation shale, including residual intergranular pores, dissolution pores, intercrystalline pores and microfractures (Fig. 6). Distinctions in pore types are evident among different lithofacies, attributed to variations in bedding

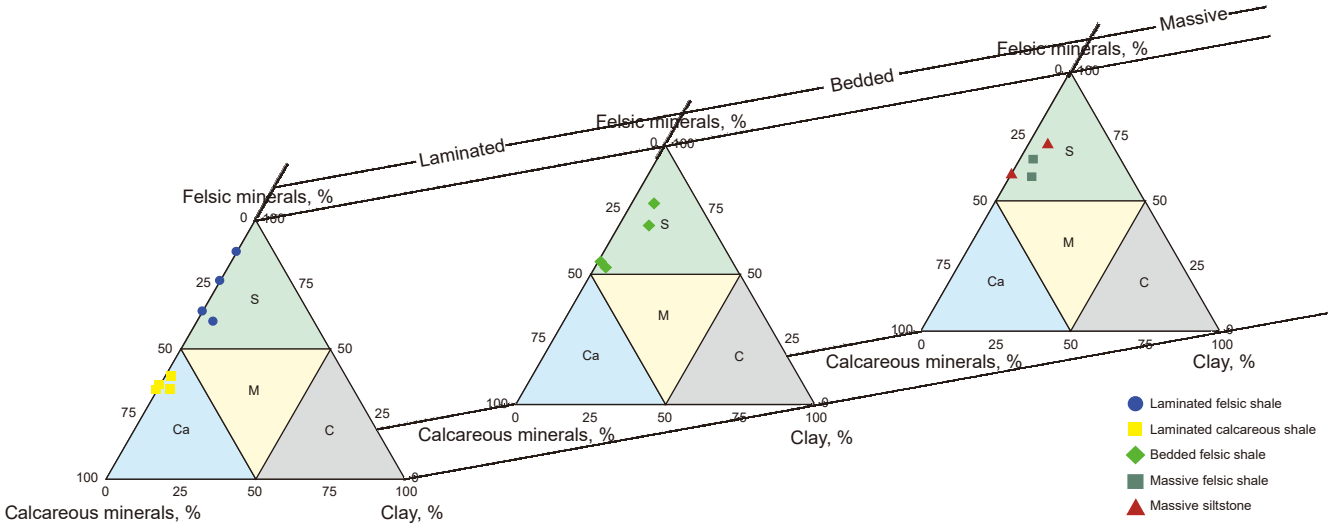

Fig. 5. Lithofacies classification of the Fengcheng Formation shale. S: siliceous; M: mixed; Ca: calcareous; C: clay-rich.

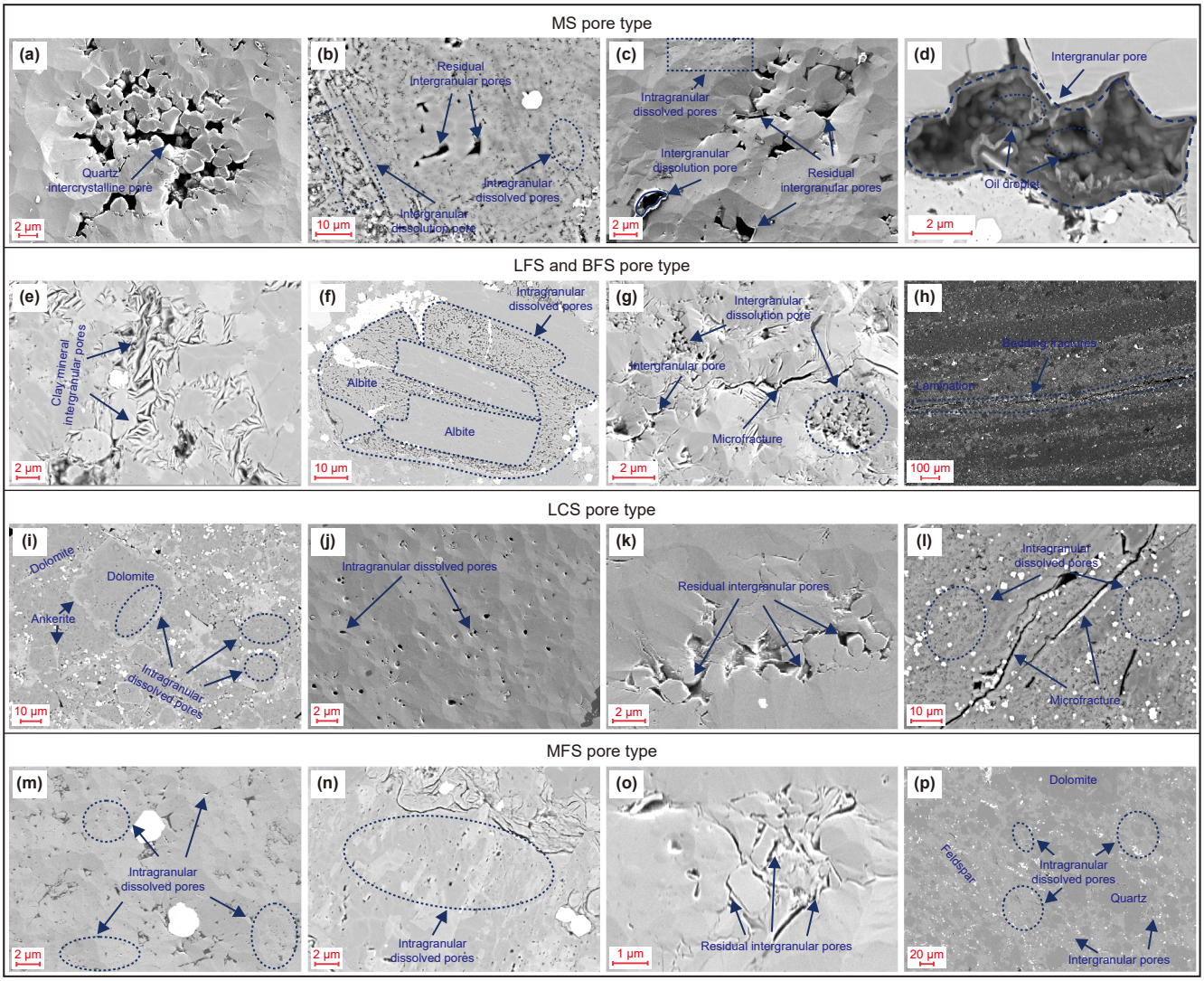

Fig. 6. Characteristics of pore type of different lithological shales. **(a)** Quartz intercrystalline pores, MY-13. **(b)** Intergranular and intragranular dissolution pores, MY-13. **(c)** Residual intergranular pores, MY-13. **(d)** Characteristics of oil occurrence in intergranular pores, MY-15. **(e)** Clay intercrystalline pores, MY-16; **(f)** Feldspar intragranular dissolution pores, MY-16. **(g)** Intergranular pores and microfractures, MY-6. **(h)** Laminated fracture, MY-14. **(i)** Dolomite intragranular dissolution pores, MY-8. **(j)** Intragranular dissolution pores, MY-3. **(k)** Residual intergranular pores, MY-2. **(l)** Microfractures, MY-7. **(m)** Intragranular dissolution pores, MY-5. **(n)** Intragranular dissolution pores, MY-12. **(o)** Residual intergranular pores, MY-5. **(p)** Feldspar intragranular dissolution pores, MY-12.

structures and mineral compositions. MS mainly develops residual intergranular pores, quartz intercrystalline pores, intergranular and intragranular dissolution pores formed by the dissolution of felsic minerals (Fig. 6(a)–(c)). These pores demonstrate favorable connectivity, with abundant oil droplets and oil films observed within them (Fig. 6(d)). LFS and BFS mainly develop intergranular pores, feldspar intragranular pores, and clay intercrystalline pores (Fig. 6(e)–(g)). During burial, residual intergranular pores and fractures are preserved under the support of felsic particles. Intragranular dissolution pores are primarily formed through acid-base reactions involving organic acids and rocks. Meanwhile, bedding-parallel microfractures develop within laminations (Fig. 6(h)), connecting intergranular pores distributed along these planes. LCS exhibits a mixed composition of felsic particles and calcareous debris, with reservoir spaces mainly comprising intragranular dissolution pores in carbonate minerals, residual intergranular pores, and microfractures (Fig. 6(i)–(l)). Notably, dolomite grains commonly feature abundant intragranular dissolution pores internally, whereas the external ferroan dolomite bands exhibit fewer dissolution pores (Fig. 6(i)). MFS demonstrates relatively poor pore development, featuring residual intergranular pores and feldspar intragranular dissolution pores, which are mostly small in size and exhibit minimal microfracture development (Fig. 6(m)–(p)).

4.2.2. Nitrogen pore morphology characteristics

The hysteresis loops observed in Fengcheng Formation samples correspond to H2, H3, and H4 types based on the IUPAC standard (Fig. 7) (Thommes et al., 2015). Among them, the hysteresis loops of MS represent a combination of H3 and H4 types, with a steep desorption curve and limited adsorption capacity, indicating predominant pore spaces in the form of plate-shaped slit pores and wedge-shaped pores (Fig. 7(a)). LFS, LCS, and BFS samples exhibit a composition of H2, H3, and H4 types with steep desorption curves and broader hysteresis loops, suggesting that not only plate-shaped slit pores and wedge-shaped pores are developed, but also a large number of ink-bottle-like pores are present (Fig. 7(d), (g) and (j)). The ink-bottle-shaped pores here primarily originate from dissolution of inorganic minerals rather than organic matter pores typically observed in overmature marine shales (Chang et al., 2024). MFS displays hysteresis loops of only H2 and H3 types, characterized by ink-bottle-shaped and wedge-shaped pores (Fig. 7(m)). Furthermore, the absence of a horizontal plateau near the saturation vapor pressure ($P/P_0 = 1.0$) in the isotherms of all samples can be attributed to the presence of larger pores in the shale samples, which extend beyond the measurable range of the experiment (Ravikovitch and Neimark, 2002).

4.2.3. NMR multi-scale PSD characteristics

The Fengcheng Formation shale samples primarily exhibits micro pore development, with an average proportion of 65.89% (Fig. 8(a)). Different lithofacies exhibit distinct PSD characteristics. MFS is predominantly composed of micropores, with micropore proportions typically exceeding 90%, while mesopores and macropores are scarcely developed (Fig. 8(b)). Similarly, BFS is primarily micropore-dominated (Fig. 8(c)), with an average proportion of 81.55%, slightly lower than that of MFS. LFS and LCS samples display significant variability in PSD (Fig. 8(d) and (e)), with fewer micropores compared to BFS and MFS, averaging 56.73%. Notably, MY-6, MY-7, and MY-10 exhibit distinct bimodal distributions, with macropores accounting for more than 30% on average, accompanied by well-developed microfractures (Fig. 6(g) and (l)). Conversely, MS shows less microfracture development but exhibits well-developed intergranular pores (Fig. 6(c)). These pores account for an average of over 50% mesopore proportions, with a concentrated and continuous PSD (Fig. 8(f)), suggesting strong connectivity between pores.

4.2.4. Fractal characteristics of movable fluid pore space

Fig. 9 illustrates the double logarithmic (V–T_2) coordinates for oil-saturated shale samples. All D_2 values fall within the range of 2–3, while certain D_1 values are below 2 (Table 2). These outliers are excluded from further discussion in this study. The range of D_1 spans 2.0254 to 2.6885, with a mean of 2.3253, whereas D_2 spans from 2.9005 to 2.9918, with a mean of 2.9578. The consistent observation that D_2 exceeds D_1 suggests that the pore space for

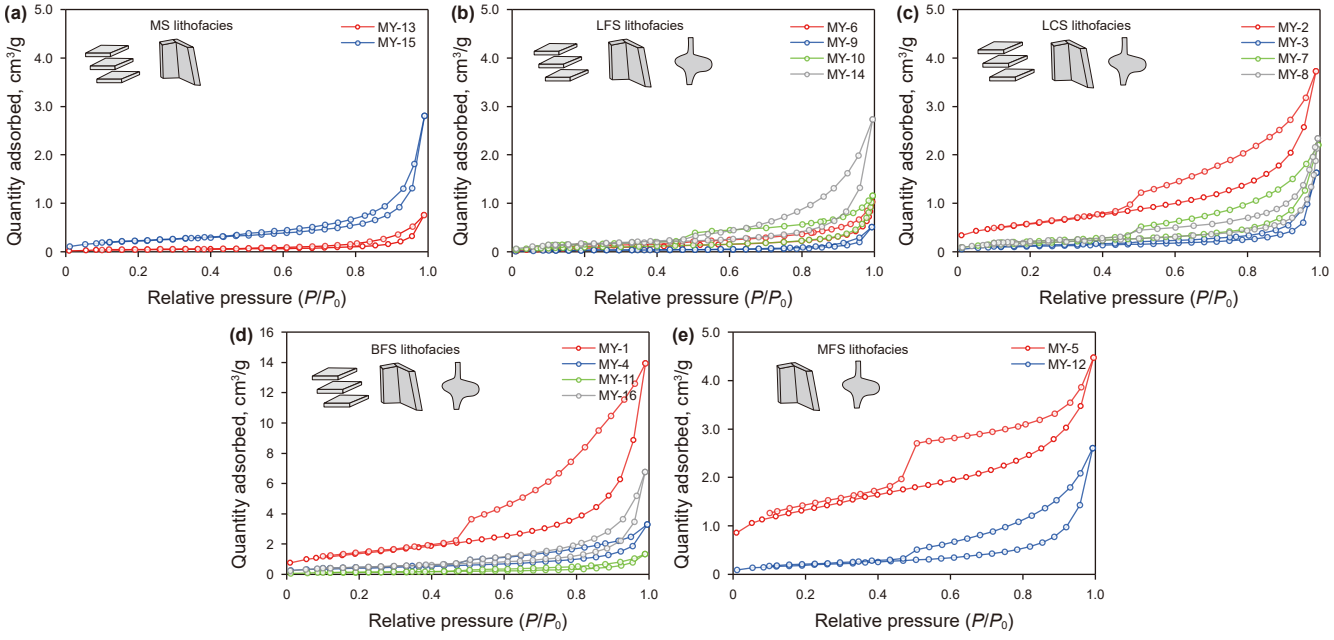

Fig. 7. Adsorption-desorption curves of different lithofacies shale obtained by NA. **(a)** MS; **(b)** LFS; **(c)** LCS; **(d)** BFS; **(e)** MFS.

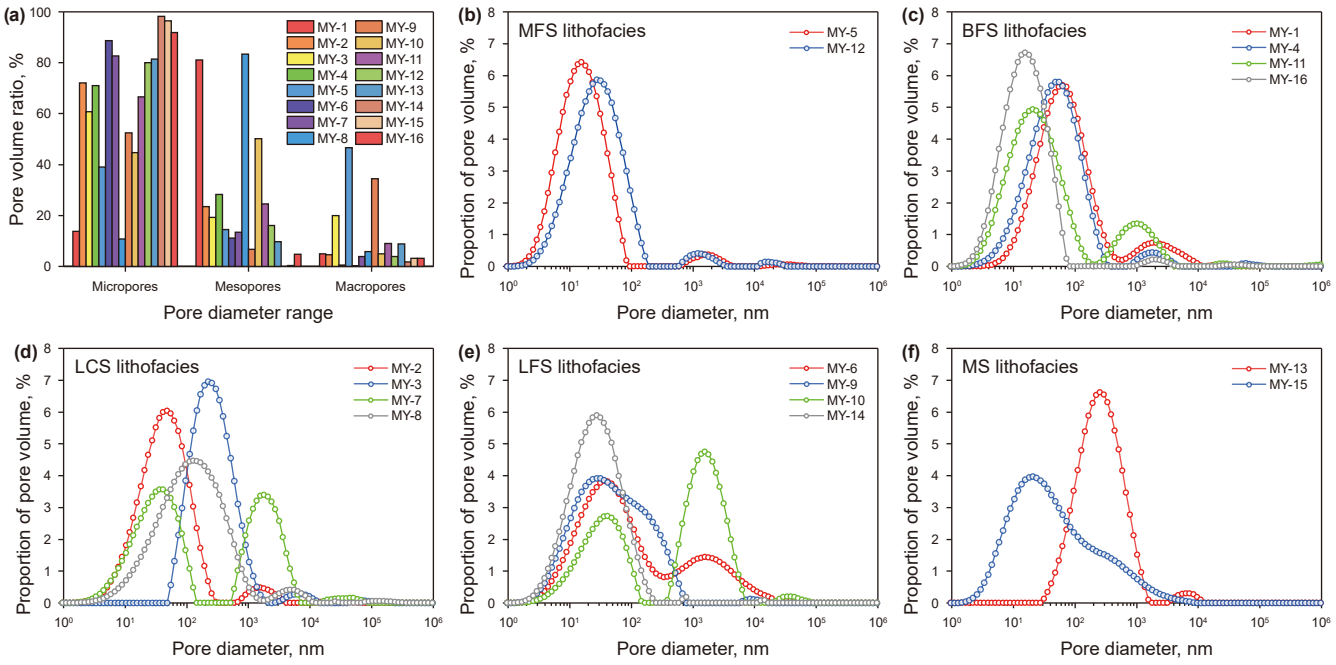

Fig. 8. NMR PSD characteristics of different lithofacies shale. **(a)**The proportion of different scales pores in shale samples; **(b)** MFS; **(c)** BFS;**(d)** LCS;**(e)** LFS;**(f)** MS.

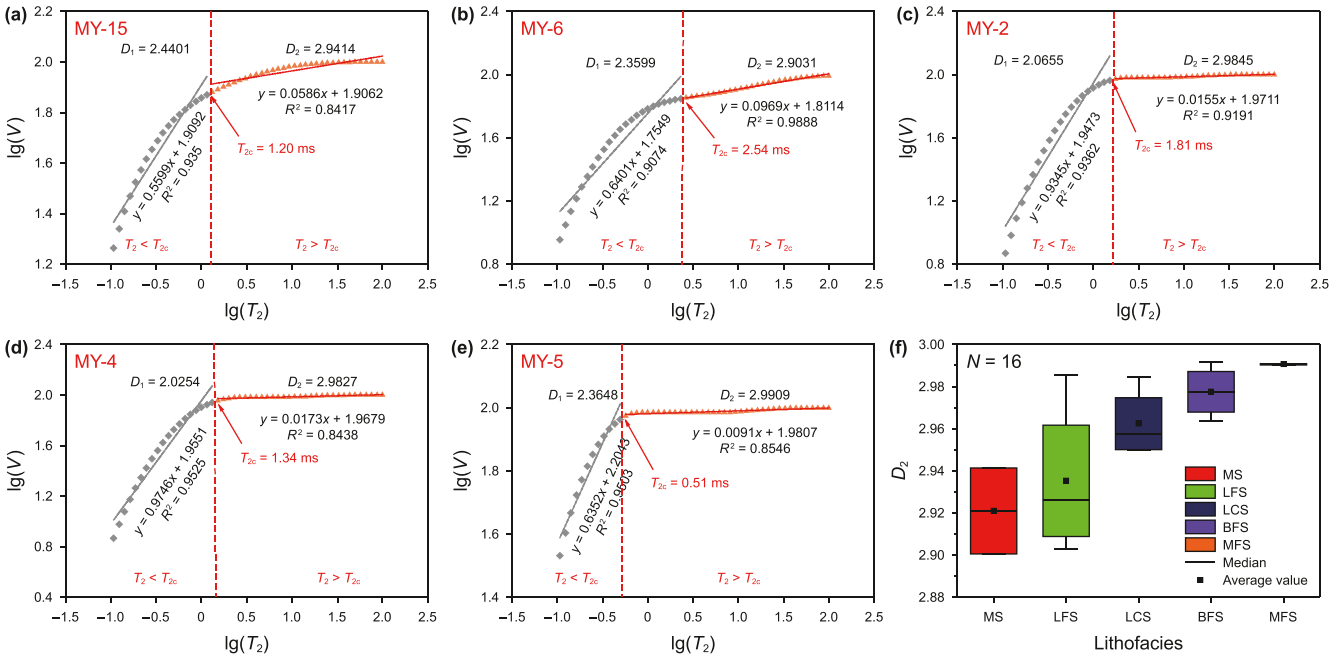

Fig. 9. Fractal characteristics of Fengcheng Formation shale samples. **(a)** MS, sample MY-15; **(b)** LFS, sample MY-6; **(c)** LCS, sample MY-2; **(d)** BFS, sample MY-4; **(e)** MFS, sample MY-5; **(f)** Box plots of D_2 distribution in different lithofacies shale.

movable fluids is more complex than that for bound fluids, corroborating previous findings (Ma et al., 2019; Sun et al., 2019). Additionally, lower D_2 values imply better pore connectivity and higher permeability in the reservoir (Zhou et al., 2022; Yang et al., 2023). The average D_2 values for different shale lithofacies follow the order: MS < LFS < LCS < BFS < MFS (Fig. 9(f)). This indicates that MS and LFS exhibit superior pore structures and higher permeability, whereas MFS have the poorest pore structures and weakest permeability.

4.3. Shale wettability detected by CAM

The shale surface wettability in the study area was investigated using oil (*n*-decane) and water (DI water) contact angle experiments, with results summarized in Table 3. During the oil droplet experiments, it was observed that when droplets contacted the rock surface, the low surface tension of the oil facilitated quick spreading, resulting in a very small gas-oil-rock contact angle. Similar phenomena have been reported in previous studies (Hu

Table 2
NMR parameters of shale samples.

Sample	Lithofacies	NMR pore size distribution ratio, %			NMR fractal dimension	
		Micropore	Mesopore	Macropore	D_1	D_2
MY-1	BFS	66.56	24.47	8.97	2.3289	2.9637
MY-2	LCS	82.72	13.40	3.88	2.0655	2.9845
MY-3	LCS	10.85	83.38	5.77	0.8497	2.9503
MY-4	BFS	79.96	16.16	3.88	2.0254	2.9827
MY-5	MFS	96.43	0.38	3.19	2.3648	2.9909
MY-6	LFS	60.71	19.31	19.98	2.3599	2.9031
MY-7	LCS	56.02	7.20	36.78	2.6885	2.9499
MY-8	LCS	44.77	50.22	5.01	2.0711	2.9649
MY-9	LFS	71.06	28.33	0.61	2.4380	2.9858
MY-10	LFS	39.01	14.40	46.58	2.6164	2.9376
MY-11	BFS	81.45	9.70	8.85	2.2885	2.9720
MY-12	MFS	91.94	4.85	3.21	1.8341	2.9903
MY-13	MS	13.84	81.17	4.99	0.4547	2.9005
MY-14	LFS	88.68	11.17	0.15	1.4260	2.9147
MY-15	MS	72.03	23.46	4.52	2.4401	2.9414
MY-16	BFS	98.22	0.00	1.78	2.2166	2.9918

et al., 2018; Wang et al., 2022). In the water droplet experiments, the gas-water-rock contact angle exhibited a stable hemispherical shape (Fig. 10). Based on the difference in water contact angles, shale reservoir wettability can be classified as strong water-wetting ($\theta < 30°$), medium water-wetting ($30° < \theta < 60°$), weak water-wetting ($60° < \theta < 90°$), weak oil-wetting ($90° < \theta < 120°$), medium oil-wetting ($120° < \theta < 150°$) and strong oil-wetting ($150° < \theta < 180°$) (Almudhhi et al., 2022). The findings revealed that the water contact angles of the shales are between 51.8° and 113.6°, with a mean of 73.8°. LFS typically exhibited smaller water contact angles, averaging 56.3°, indicating medium water-wetting. In contrast, MS displayed water contact angles exceeding 100°, significantly higher than those of other samples, demonstrating obvious weak oil-wetting characteristics.

4.4. Characteristics of shale pore connectivity based on SI

The SI process has two distinct stages (Fig. 11). Initially, during the early imbibition, the liquid rapidly penetrates the pore space under the influence of strong capillary forces, resulting in a phase of swift growth. Subsequently, as fluid saturation increases, capillary forces weaken, leading to a stable growth phase as the fluid slowly permeates the pores. The slope in the log-log plot of cumulative imbibition amount versus time serves as an indicator of pore connectivity, with higher slope values signifying better connectivity. Imbibition results demonstrate that the slope for oil is obviously higher than that for water (Fig. 11), indicating that the oil-wet pore connectivity of the samples is superior to their water-wet pore connectivity.

The imbibition slopes vary across different shale lithofacies. MS and laminated shale exhibit higher imbibition slopes, suggesting relatively better connectivity. BFS follows, while MFS shows the lowest imbibition slopes, signifying the poorest connectivity (Fig. 11). The MS samples (MY-13 and MY-15) display oil imbibition slopes as high as 0.654 and 0.571, respectively (Fig. 11(a)), surpassing those of other lithofacies. This can be attributed not only to their strong pore connectivity but also to their oleophilic nature, resulting in faster oil imbibition and higher oil slopes. Laminated shale, characterized by more developed microfractures, facilitates the formation of pore-fracture network systems, enhancing pore connectivity and yielding higher imbibition slopes. Moreover, the oil imbibition slopes of LFS consistently exceed 0.5 (Fig. 11(b)), higher than those of LCS (Fig. 11(c)). This difference likely arises from the calcareous shale's predominant development of ink-bottle-shaped dissolution pores, which exhibit poor connectivity and hinder fluid imbibition.

4.5. Movable oil content and saturation detected by the MTP Rock-Eval and NMR

4.5.1. Characterisation of movable oil content from geochemical perspective

The total oil content of samples ranges from 0.06 to 8.3 mg/g, with a mean of 3.55 mg/g, while the movable oil content spans from 0.04 to 5.04 mg/g, exhibiting a wider distribution and a mean of 1.21 mg/g. As shown in Fig. 12, movable oil content is notably lower in MFS and BFS samples, averaging 0.37 mg/g. Among these, sample MY-5 exhibits the lowest movable oil content and the poorest mobility. Conversely, two MS samples exhibit the highest values for both movable and total oil content, with movable oil accounting for over 60% of the total, indicating strong mobility. In MS samples, the movable oil content is significantly larger than the adsorbed oil content, whereas other shale samples are predominantly characterized by adsorbed oil. This is because light hydrocarbons, with lower density and viscosity, more easily migrate from adjacent shale layers into the siltstone interbeds. In contrast, the shale retains a substantial amount of immobile heavy hydrocarbons and thermally released kerogen hydrocarbons.

Table 3
Water and oil contact angle and SI results of shale samples.

Sample	Lithofacies	Contact angle of DI water, °	Contact angle of *n*-decane, °	DI water SI slope	*n*-decane SI slope
MY-1	BFS	63.8	<15	0.228	0.418
MY-2	LCS	58.8	<15	0.284	0.382
MY-3	LCS	65.3	<15	0.295	0.510
MY-4	BFS	78.8	<15	0.303	0.379
MY-5	MFS	90.8	<15	0.103	0.123
MY-6	LFS	51.8	<15	0.291	0.521
MY-7	LCS	74.8	<15	0.361	0.460
MY-8	LCS	73.7	<15	0.334	0.502
MY-9	LFS	54.8	<15	0.296	0.548
MY-10	LFS	58.2	<15	0.320	0.570
MY-11	BFS	89.2	<15	0.160	0.271
MY-12	MFS	83.8	<15	0.209	0.125
MY-13	MS	113.6	<15	0.386	0.654
MY-14	LFS	60.3	<15	0.376	0.526
MY-15	MS	105.7	<15	0.235	0.571
MY-16	BFS	57.5	<15	0.335	0.436

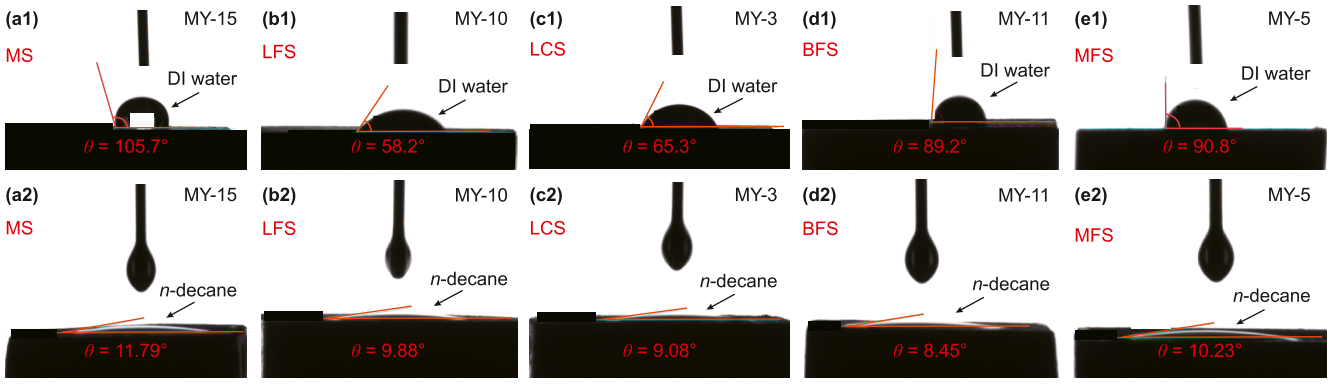

Fig. 10. Water and oil contact angle characteristics of typical shale samples. **(a)** MS, sample MY-15; **(b)** LFS, sample MY-10; **(c)** LCS, sample MY-3; **(d)** BFS, sample MY-11; **(e)** MFS, sample MY-5.

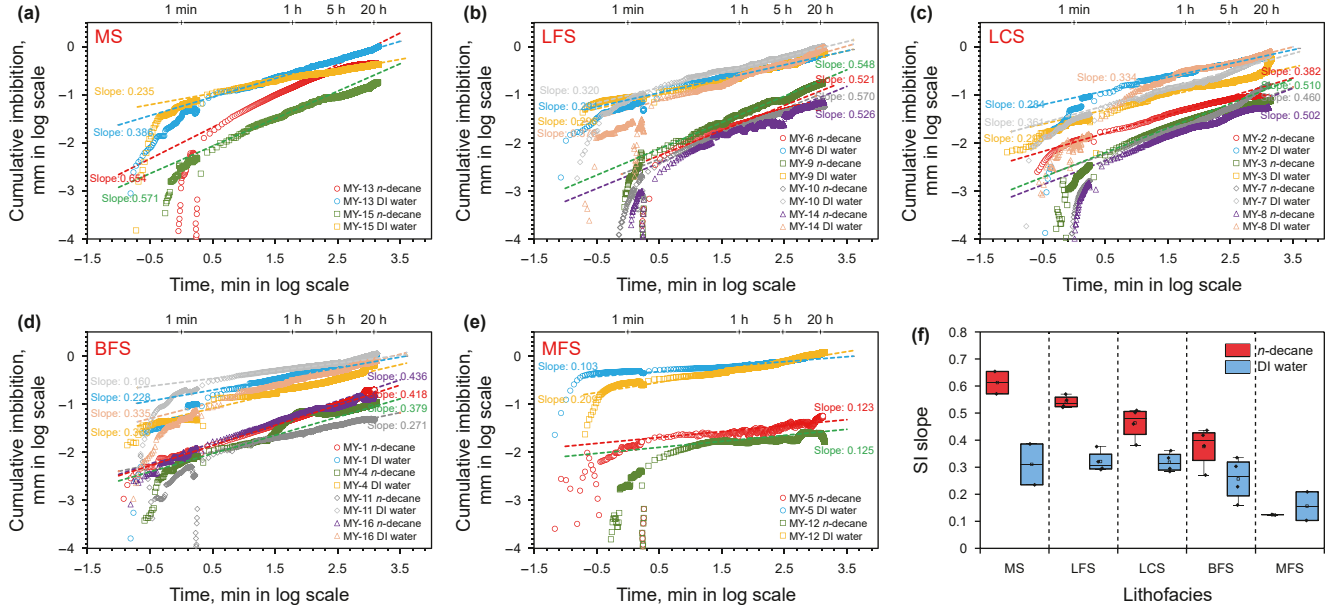

Fig. 11. SI characteristics of oil and water of different lithofacies shale. **(a)** MS; **(b)** LFS; **(c)** LCS; **(d)** BFS; **(e)** MFS; **(f)** box plots of SI slopes of different lithofacies shale.

4.5.2. Characterisation of movable oil saturation from reservoir perspective

Fig. 13 illustrates the distribution characteristics of adsorbed oil, free oil, and movable oil in typical shale samples from the Fengcheng Formation. The dark blue area represents the T_2 spectrum under saturated conditions, and the green area represents the T_2 spectrum after centrifugation. The gap between them corresponds to the movable oil, as determined from direct experimental measurements. In contrast, the adsorbed oil in the red region and the free oil in the light blue region (representing the maximum potentially movable oil content) are derived from theoretical calculations based on the adsorption ratio model (Eq. (4)). Free oil predominantly resides in mesopores and macropores, while oil in micropores primarily exists in the form of adsorbed oil, aligning with the findings of Zhang et al. (2022). Notably, a considerable amount of residual oil remains bounded in the free oil region after centrifugation, indicating that not all free oil is movable under experimental conditions. Additionally, movable oil is not strictly confined to the theoretically calculated free oil fraction but also appears in the adsorbed oil region. This phenomenon suggests that the boundary between adsorbed and free oil is not absolute, and some adsorbed oil may exhibit a degree of mobility.

The movable oil saturation (S_m) for all samples, as shown in Table 4, range from 7.7% to 44.6%, with an average of 20.0%. The S_m values of different lithofacies vary greatly. The MS exhibits the highest S_m, averaging 35.2%, followed by LFS and LCS, averaging 25.9% and 19.2%, respectively. BFS and MFS show lower S_m values, averaging 12.9% and 8.5%. The S_m within micropores, mesopores, and macropores was obtained separately to elucidate the differences in fluid mobility across various scales pores. The movable oil of MFS is predominantly distributed in micropores, accounting for up to 87.8% (Fig. 13(a)). Since oil in micropores is primarily adsorbed oil, most fluids cannot flow freely, resulting in lower S_m in shale with a high proportion of micropores. In contrast, BFS exhibits a shift of the main peak to the right (Fig. 13(b)), with a reduced S_m of micropore, averaging 54.8%, and an increased S_m of mesopore, averaging 30.4%. In laminated shales (LCS and LFS), movable oil primarily resides in mesopores, with an average S_m of 41.5%, and macropores also show relatively high S_m, averaging 25.2%. Among them, the T_2 spectrum of LCS sample MY-7 displays a discontinuous bimodal distribution, with movable oil primarily

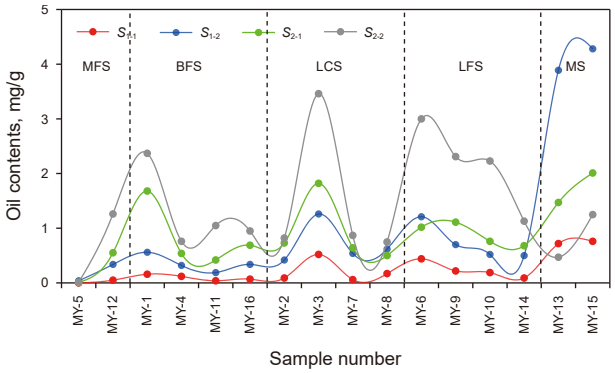

Fig. 12. Different types of oil content of shale samples obtained by MTP.

in the right peak (Fig. 13(c)), yielding an S_m of 21.3%. In contrast, LFS sample MY-6 achieves an S_m as high as 29%, with a continuous bimodal T_2 spectrum and well-developed microfractures (Fig. 6(g)). The right peak likely corresponds to fluid signals associated with these microfractures (Zhao et al., 2022). Significant changes in T_2 spectra before and after centrifugation are observed in the multiscale pores (Fig. 13(d)), possibly due to microfractures connecting different dimensions pores. The NMR T_2 signal of MS sample MY-13 decreases sharply after centrifugation (Fig. 13(e)), resulting in an S_m as high as 44.6%. The movable oil is primarily distributed in mesopores, with an average proportion of 70.7%. This high mobility is attributed to the well-sorted pores and the development of connected intergranular pores (Fig. 6(a)–(c)).

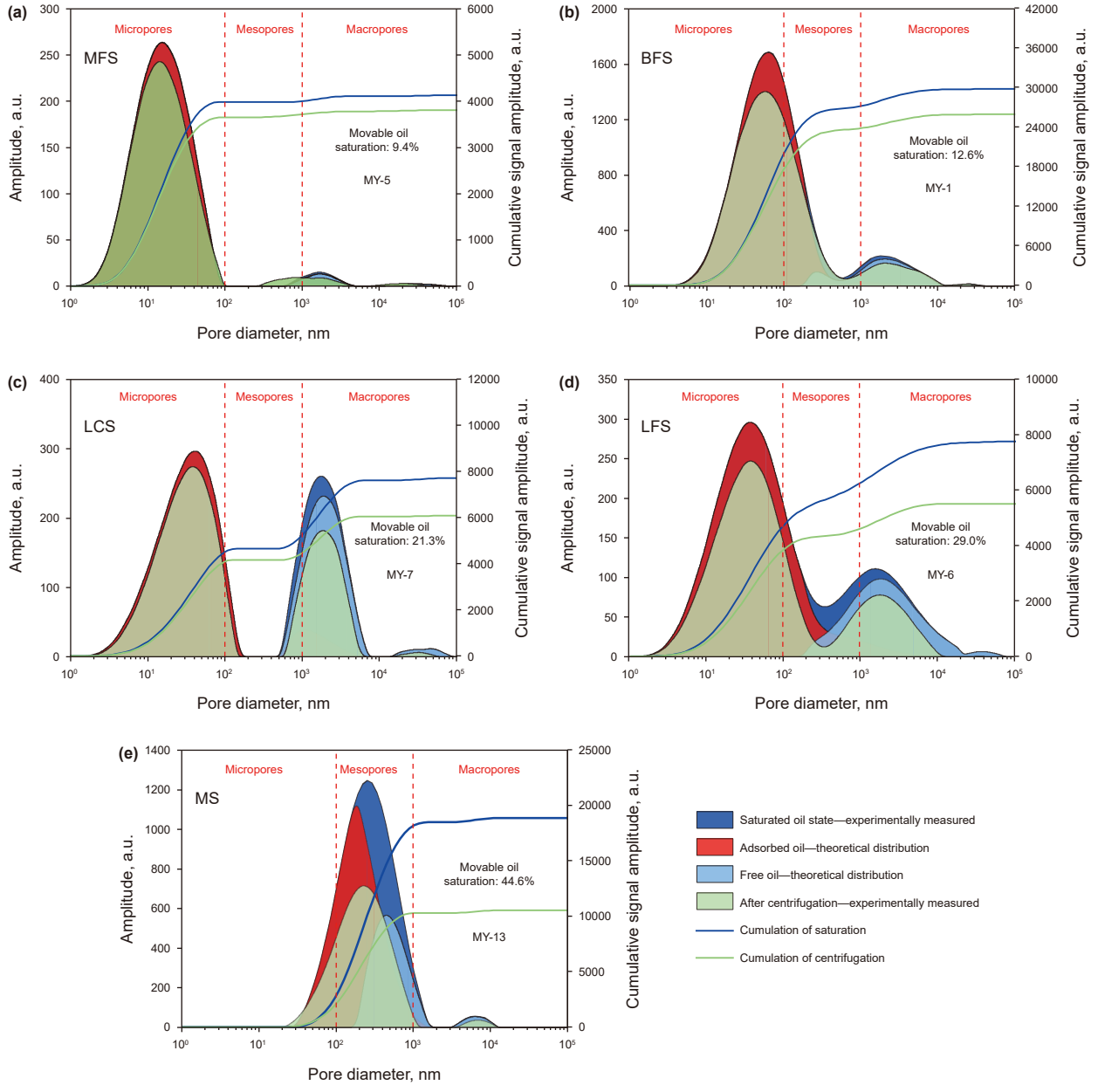

Fig. 13. NMR distribution characteristics of shale oil in different occurrences states. **(a)** MFS, sample MY-5; **(b)** BFS, sample MY-1; **(c)** LCS, sample MY-7; **(d)** LFS, sample MY-6; **(e)** MS, sample MY-13.

Table 4
Moveable oil saturation parameters in different scale pores of shale.

Sample	Lithofacies	Movable oil saturation, %	Proportion of movable oil in different pores, %		
			Micropores	Mesopores	Macropores
MY-1	BFS	12.6	57.9	27.1	15.0
MY-2	LCS	14.3	51.6	38.5	9.9
MY-3	LCS	24.6	3.0	79.2	17.8
MY-4	BFS	13.7	53.4	38.8	7.8
MY-5	MFS	9.4	87.8	0.0	12.2
MY-6	LFS	29.0	38.3	34.1	27.6
MY-7	LCS	21.3	24.6	18.3	57.1
MY-8	LCS	16.4	8.8	69.3	21.9
MY-9	LFS	25.6	59.2	39.6	1.2
MY-10	LFS	15.8	14.9	19.8	65.3
MY-11	BFS	10.6	9.9	55.6	34.5
MY-12	MFS	7.7	73.7	11.0	15.3
MY-13	MS	44.6	8.7	83.2	8.1
MY-14	LFS	33.2	65.5	33.5	1.0
MY-15	MS	25.8	30.0	58.2	11.8
MY-16	BFS	14.7	97.9	0.0	2.1

5. Discussion

5.1. The influencing factors of shale oil mobility

5.1.1. The influence of pore structure, connectivity and wettability on movable oil saturation

The research area's shale oil mobility exhibits significant variation, with S_m values differing considerably due to multiple controlling factors (Fig. 14(a)). The findings reveal a significant positive relationship between S_m and both porosity and permeability (Fig. 14(b) and (c)), with Pearson correlation coefficients reaching 0.8 and 0.81, respectively. This result aligns with expectations that the higher porosity and permeability enhance the reservoir capacity and fluid flow capability, facilitating fluid mobility and increasing S_m values. However, it is noteworthy that in shale samples with permeability below 0.005×10^{-3} μm^2, the relationship between S_m and permeability becomes less distinct (Fig. 14(c)), and some samples demonstrate "low-permeability, high-S_m" phenomenon. This suggests that in ultra-low-permeability shale, the complexity of the pore structure hinders accurate predictions of fluid mobility, indicating that S_m may not be controlled by a single factor.

Differences in pore structure influence the adsorption capacities of shale oil, thereby controlling its mobility (Zhang et al., 2022). Smaller pores result in stronger solid-liquid interactions, leading to thicker adsorbed oil films on pore walls, which restrict fluid mobility (Li et al., 2024a). Conversely, larger pores indicate a reduced ratio of adsorbed oil while increasing free oil ratio, thereby enhancing the movable oil ratio (Song et al., 2024). The S_m is positively correlated with the percentage of pores volume larger than 100 nm (Fig. 14(d)), indicating that shale oil mobility in the study area is controlled by the development of mesopores and macropores. These larger pores, with smaller specific surface area and lower capillary forces, are more conducive to shale oil flow compared to micropores. Nanopore morphology also affects fluid flow capacity. Compared to cylindrical pores, slit pores exhibit superior flow capacity (Zhao et al., 2024). Consequently, shales with H4-type plate-shaped slit pores demonstrate better flowability than those dominated by H2-type ink-bottle pores. Fig. 14(e) and (f) illustrate the relationship between fractal dimensions and S_m. While the correlation between the D_1 and S_m is insignificant, the D_2 exhibits a pronounced negative correlation with S_m, with a Pearson correlation coefficient as high as 0.82. This suggests that the pore structure of movable fluids is closely linked to shale oil mobility. An increase in D_2 signifies a more complex pore space for movable fluids, characterized by greater surface roughness and uneven pore distribution (Sun et al., 2019). A rougher pore surface enhances fluid adsorption capacity, causing more oil to be retained in pores. Furthermore, complex pore structures restrict fluid flow channels (Zhang et al., 2020), impeding shale oil mobility and reducing S_m. This finding align with numerous recent studies (Yang et al., 2023; Li et al., 2024a; Wu et al., 2024), confirming the validity of NMR fractal dimension in characterizing shale reservoir pore structures and its influence on fluid mobility.

The seepage capacity of shale reservoir is directly determined by pore connectivity. Fig. 14(g) and (h) show a clear positive correlation between S_m and both oil and water SI slopes, indicating that better pore connectivity enhances shale oil mobility. However, the correlation between S_m and the oil SI slope is stronger than that with the water SI slope (Fig. 14(a)), primarily due to differences in oil and water wettability. In hydrophilic shales, water-wet pores exert a repulsive effect on the oil phase, hindering oil flow (Lan et al., 2015; Wang et al., 2022). Therefore, the SI slope of a similar-phase fluid (oil phase) more effectively reflects oil mobility and shows a stronger correlation with S_m. While the SI slope of water also reflects pore connectivity, competitive adsorption between water and oil weakens its correlation with S_m.

Shale wettability directly control fluid distribution and flow behavior in the pore space, thereby influencing shale oil mobility (Afekare et al., 2021; Shi et al., 2022). As the water contact angle decreases, S_m gradually increase (Fig. 14(i)), suggesting that water-wet shales exhibit higher oil mobility (Lin et al., 2024; Xu et al., 2024). This is because oil-wet conditions enhance the oil adsorption capacity of pore walls, leading to higher proportion of adsorbed oil within the pore space, which subsequently reduces the ratio of movable oil. Notably, the MS has not been considered here. Because the MS has significantly larger pores than the other shale samples, its mobility is primarily controlled by pore size rather than wettability.

5.1.2. The influence of geochemical characteristics on shale oil mobility

Organic matter abundance serves as the foundation for shale oil formation and enrichment (Jiang et al., 2023). As illustrated in Fig. 15(a), both adsorbed oil and movable oil content exhibit a positive correlation with TOC, indicating that higher TOC content, the more adsorbed oil and movable oil. The relationship between

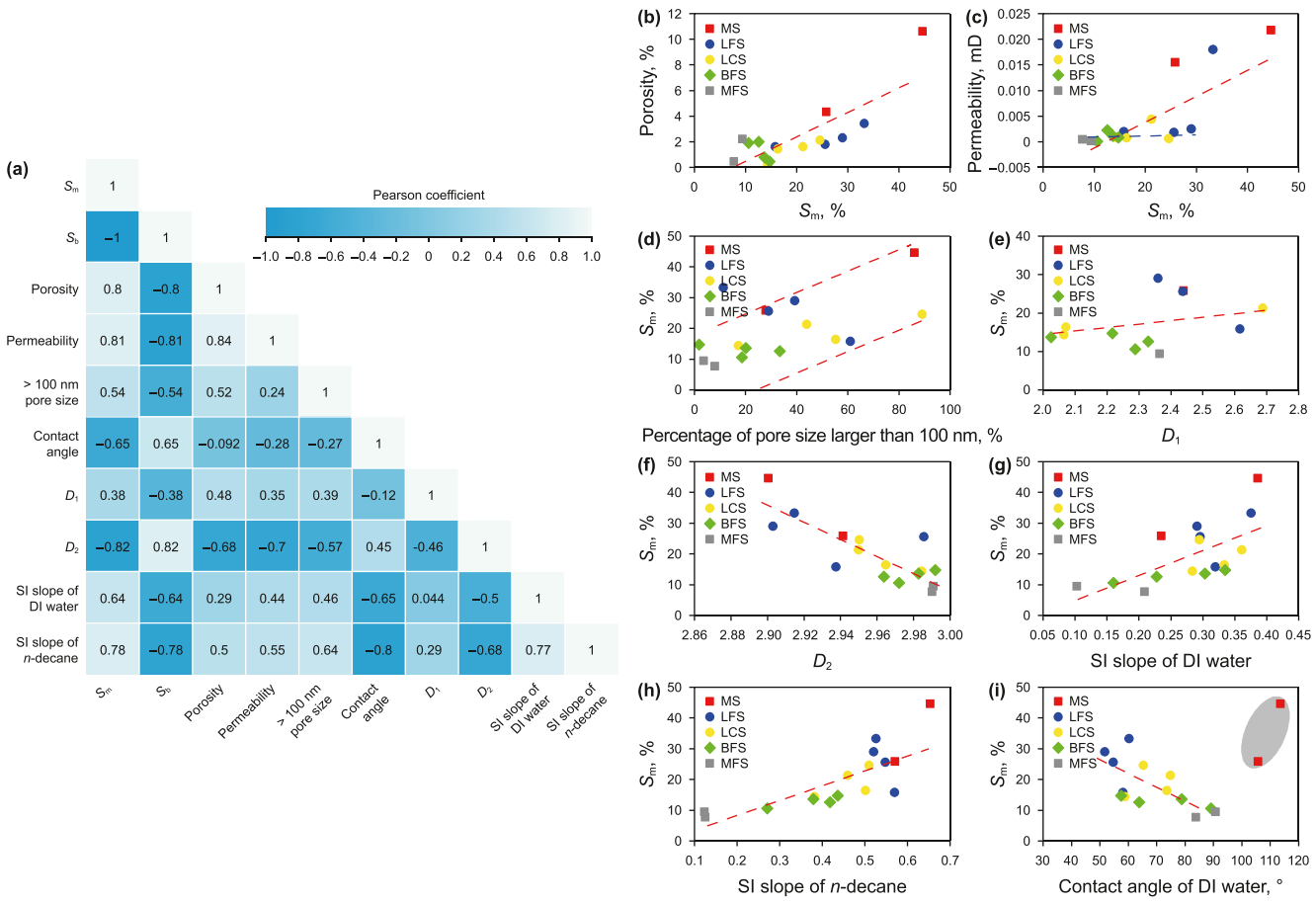

Fig. 14. Influence of shale pore structure, connectivity and wettability on S_m. **(a)** Pearson correlation matrix of multiple influences controlling for S_m. **(b)** Crossplot of porosity and S_m. **(c)** Crossplot of permeability and S_m. **(d)** Crossplot of percentage of pore size (>100 nm) and S_m. **(e)** Crossplot of D_1 and S_m. **(f)** Crossplot of D_2 and S_m. **(g)** Crossplot of SI slope of *n*-decane and S_m. **(h)** Crossplot of SI slope of DI water and S_m. **(i)** Crossplot of contact angleand S_m.

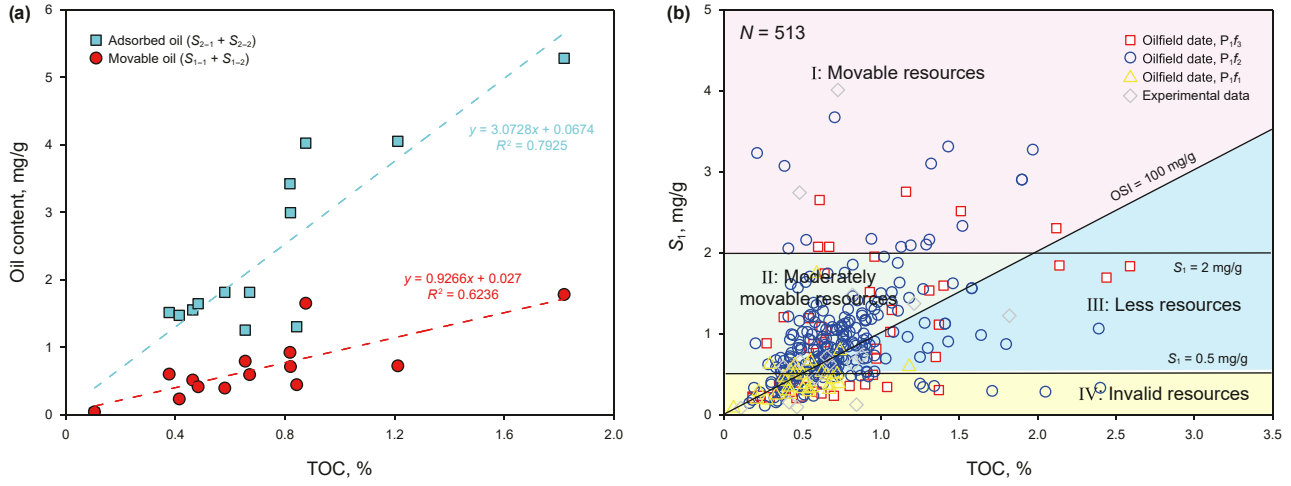

Fig. 15. Influence of geochemical parameters on the shale oil mobility in the Fengcheng Formation. **(a)** The relationship between adsorbed and movable oil content and TOC. **(b)** Cross-plot of S_1 with TOC.

TOC and adsorbed oil content is particularly pronounced, as the strong adsorption of oil molecules by organic matter causes adsorbed oil content to rise with increasing TOC. However, when shale oil reaches the volume limit of the pore space, excessively high TOC levels hinder the mobility of shale oil (Tian et al., 2024). In the Beibu Gulf Basin, where the shale oil is in a mature stage, the average TOC content is relatively high (4.2%), and movable oil content shows a negative correlation with TOC (Nie et al., 2024). This occurs because, beyond a threshold, the influence of TOC on shale oil content becomes negligible (Zhao et al., 2020). At

constant oil volume, increased TOC elevates adsorbed oil content, thereby reducing the amount of movable oil. However, in the Fengcheng Formation, where TOC content is generally low, this threshold has not been reached, and the adverse effects of high TOC levels on movable oil are not yet evident.

OSI, defined as the ratio of free hydrocarbons (S_1) to TOC, is a commonly used geochemical parameter to evaluate shale oil mobility (Song et al., 2024; Xiao et al., 2024). When the generated hydrocarbons exceed adsorption capacity and reservoir saturation, excess hydrocarbons are expelled, resulting in the "oil crossover effect" (Jarvie, 2012). Based on this concept, an OSI value of 100 mg/g is typically used as an empirical threshold for shale oil mobility (Jarvie, 2012; Li et al., 2021; Zhu et al., 2024). In this study, combining the evaluation of shale oil resource potential by Wu et al. (2022), S_1 and OSI were used to classify movable oil resources in the Fengcheng Formation into four categories (Fig. 15(b)): Type I (movable resources, OSI > 100 mg/g, S_1 > 2 mg/g); Type II (moderately movable resources, OSI>100 mg/g, 0.5 mg/g < S_1 < 2 mg/g); Type III (less resources, OSI < 100 mg/g, S_1 > 0.5 mg/g); Type IV (invalid resources, OSI < 100 mg/g, S_1 <0.5 mg/g). The MS typically exhibit high S_1 (>2 mg/g) and OSI values (>400 mg/g), classifying them as Type I movable resources. Statistical analysis reveals that the study area comprises 60.1% movable oil resources, 18.5% low-efficiency resources, and 21.4% invalid resources. Among these, the P_1f_2 shale oil, formed during the peak phase of hydrocarbon generation in the alkaline lake, contributes 45% of the movable oil resources.

5.1.3. The influence of lamination development on shale oil mobility

The development of lamination has significantly affected on shale oil mobility. The S_m follows the order (Fig. 16(a)): laminated shale > bedded shale > massive shale. Compared to massive and bedded shale, laminated shale samples exhibit a pronounced right peak of T_2 spectrum (Fig. 8(b) and (c)), indicating that macropores and microfractures are relatively more developed. During high-speed centrifugation, the capillary forces acting on macropores and microfractures are weaker, facilitating the release of movable oil (Zhu et al., 2021). The development of lamination in shale markedly enhances reservoir properties (Jiang et al., 2020; Woo et al., 2021; Xin et al., 2022). In the Fengcheng Formation shale, microfractures are frequently observed within lamination (Fig. 6(h)), aligning along bedding planes and exhibiting strong continuity, whereas such fractures are rarely present in massive shale. The presence of microfractures greatly improves reservoir connectivity, forming a percolating network that enhances shale permeability, thereby increasing the flow capacity of fluids in the pore space (Ougier-Simonin et al., 2016; Teixeira et al., 2017; Zhang et al., 2024a). These microfractures developed between lamination are generally of non-tectonic origin such as diagenesis and hydrocarbon generation, and are mainly formed under fluid overpressure induced by clay mineral dehydration and formation overpressure caused by hydrocarbon generation (Bruce, 1984; Liu et al., 2017; Chauve et al., 2020; Meng et al., 2021).

The occurrence state of shale oil is closely related to its mobility, with this relationship being particularly pronounced between lamination and the matrix. The shale matrix, typically rich in organic matter and clay minerals, serves as the primary site for hydrocarbon generation (Salmon et al., 2000; Rahman et al., 2017). Hu et al. (2024) revealed that under the driving force of capillary pressure, hydrocarbons generated in the dark matrix undergo micro-migration, preferentially accumulating in the bright lamination with relatively superior pore structures. This micro-migration results in an increased proportion of light oil in the lamination, thereby enhancing the mobility of shale oil (Sun et al., 2025). Previous studies have confirmed that this phenomenon exists in the Fengcheng Formation shale by employing laser confocal microscopy imaging technology (Gao et al., 2023; Gong et al., 2023). In the laminated shales, bright lamination are observed to contain higher light oil content (Fig. 16(c) and (f)), which possess relatively greater mobility and are easier to migrate and flow under capillary forces. In contrast, the dark matrix predominantly contains heavy oil (Fig. 16(d) and (g)), characterized by higher adsorption capacities and complex pore structures that constrain fluid mobility. Consequently, the development of lamination in shales not only facilitates the enrichment of shale oil but also significantly improves its mobility.

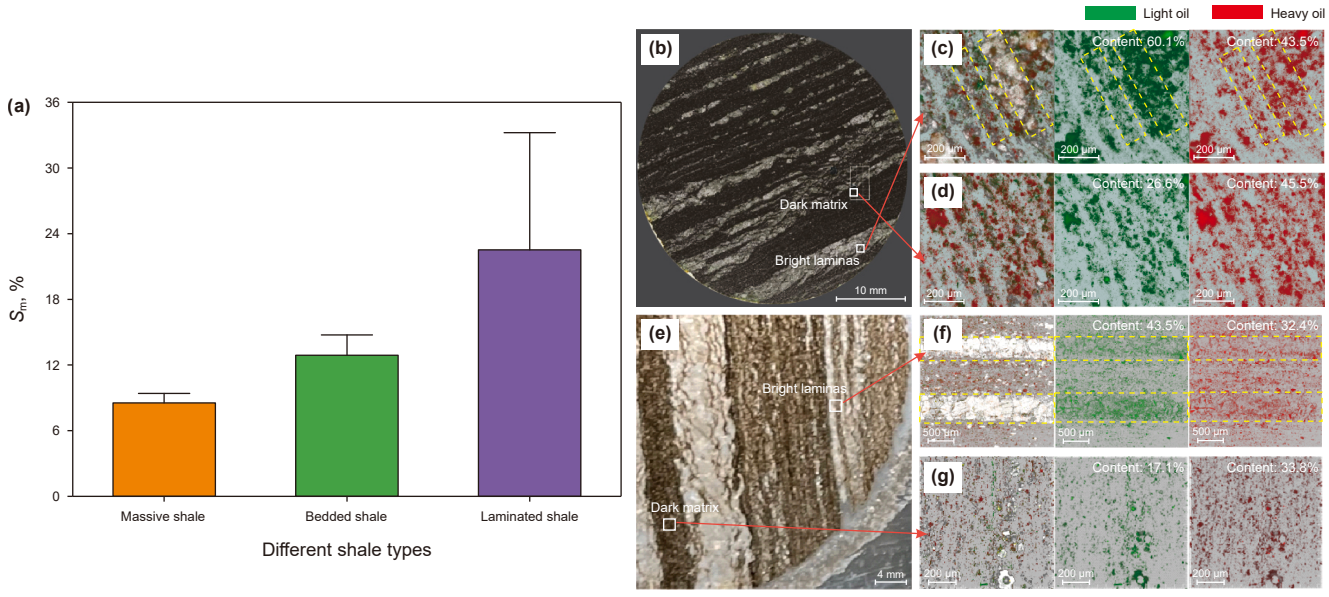

Fig. 16. **(a)** The S_m of shales with different sedimentary structure types. **(b)** Characteristics of light and heavy components in shale matrix and lamination under laser confocal microscopy (Adapted with permission from reference (Gao et al., 2023; Gong et al., 2023)).

5.2. The evaluation method of shale oil mobility

5.2.1. The movable oil content evaluation

Based on the above analyses, accurately evaluating shale oil mobility necessitates a comprehensive consideration of both the movable oil content and the pore structure of the reservoir. However, the movable oil content parameter derived from MTP primarily reflects the content of free oil (Wang et al., 2019b). Free oil, however, is not entirely equivalent to movable oil, as its actual mobility is influenced by complex pore structures and connectivity of the shale (Li et al., 2020; Nie et al., 2024). Similarly, The S_m obtained from NMR and centrifugation experiments merely indicate the efficiency of fluid mobilization in the reservoir space and cannot directly quantify the actual movable oil content. To provide a more overall assessment of shale oil mobility, this study proposes a novel method that integrates total oil content and movable oil saturation:

$$Q_{mov} = Q_t \times S_m \tag{7}$$

where Q_{mov} is actual movable oil content; Q_t is total oil content.

This approach corrects the potential overestimation of movable oil content when relying solely on MTP. The results indicate that the $S_{1\text{-}1} + S_{1\text{-}2}$ generally exceeds Q_{mov}, indicating that a portion of the free oil remains trapped in the reservoir pore space and is immobile. Furthermore, a strong correlation is observed between Q_{mov} and $S_{1\text{-}1} + S_{1\text{-}2}$ further validates the effectiveness of this method in reflecting the occurrence of movable oil (Fig. 17(a)). Additionally, Q_{mov} exhibits a significant positive correlation with porosity, permeability, oil SI slope, and the proportion of mesopores and macropores, while displaying a negative correlation with water contact angle and D_2 (Fig. 17(b)). These findings are consistent with the analysis in Section 5.1.1, indicating that shale oil mobility is governed by reservoir properties, pore heterogeneity, connectivity, and the development of mesopores and macropores. The Q_{mov} values for different lithofacies exhibit the following order: MS > LFS > LCS > BFS > MFS (Fig. 17(c)). This integrated approach more accurately reflects the actual movable oil content in shale, providing a accurate basis for the evaluation of movable resources of shale oil. However, it should be noted that this model may still have some uncertainties when applied to real formations with complex multiphase fluid systems. Specifically, the NMR-derived movable oil saturation is for a single-component fluid system, which does not fully account for the effects of bound water, structural water, or capillary-bound fluids that commonly coexist with oil in shale reservoirs. The presence of these water components may affect the mobility of oil, especially under oil–water coexisting conditions. As such, although the method provides a more representative estimation of movable oil content than traditional approaches, its applicability may be limited under complex geological settings with multiphase fluid interactions.

5.2.2. Quantitative estimation model for shale oil mobility

Regression analysis is commonly used to construct estimation models for movable oil content under the influence of multiple factors (Hu et al., 2021). In this study, IBM SPSS Statistics 27 was used to perform multiple regression analysis on various factors affecting shale oil mobility in the Fengcheng Formation of the Mahu Sag, and to establish a predictive model for movable oil content. Given the diverse factors influencing oil mobility, variables with pearson coefficients greater than 0.7 were selected to ensure model accuracy. These include porosity, permeability, SI slope of *n*-decane, movable oil pore fractal dimension (D_2), and TOC. Based on these, a quantitative prediction model for movable oil content was established as follows (Eq. (8)):

$$Y = 0.218 \times X_1 + 1.292 \times X_2 - 1.333 \times X_3 + 1.381 \times X_4 + 0.519 \times X_5 + 3.303 \tag{8}$$

where X_1 is porosity, %; X_2 is permeability, mD; X_3 is D_2; X_4 is SI slope of *n*-decane; X_5 is TOC, %.

Numerical simulation results show that the regression model achieves an R^2 value of 0.829, and the standardized residuals follow a normal distribution (Fig. 18), confirming the reliability of the model. Furthermore, the predicted movable oil contents of different lithofacies shale in the Fengcheng Formation were calculated using this model. As shown in Fig. 19, the predicted movable oil contents exhibit strong positive correlations with key shale oil mobility indicators, including Q_{mov}, S_m and $S_{1\text{-}1} + S_{1\text{-}2}$, further validating the model's practicability.

5.3. Mobility conceptual models of shale oil in different lithofacies

In the Mahu Sag, variations in depositional environments, such as paleoclimate, sediment supply, and astronomical cycles, exert significant control over bedding structures and mineral components (Wang et al., 2021; Huang et al., 2023). These differences in bedding structures and mineral components form five different lithofacies in the Fengcheng Formation shale system (Fig. 20(a)). These lithofacies exhibit variations in reservoir space types and properties, which are key factors influencing movable oil saturation. This study systematically examines the pore structures,

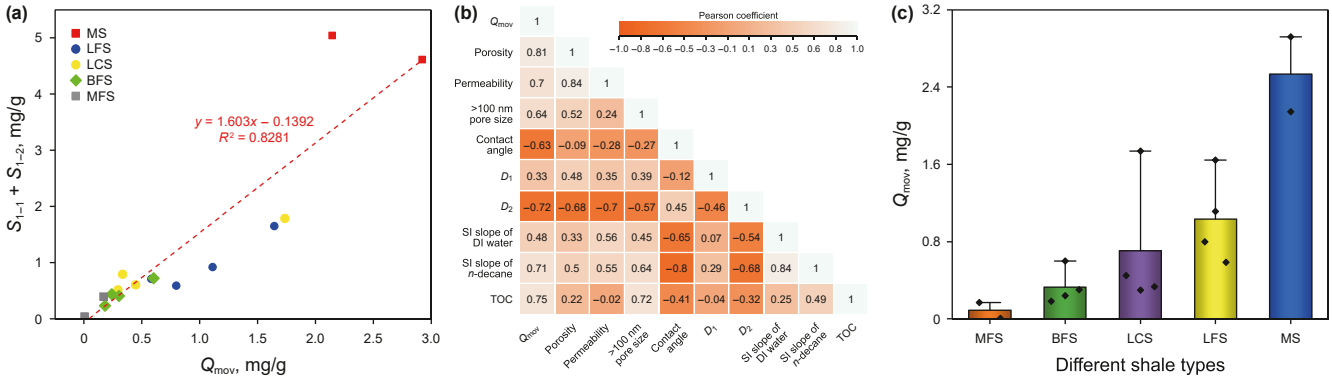

Fig. 17. **(a)** Correlation between the $S_{1\text{-}1}$+$S_{1\text{-}2}$ obtained from MTP experiments and Q_{mov} calculated from the new method; **(b)** Pearson correlation matrix of pore structure, connectivity, wettability parameters and Q_{mov}; **(c)** The Q_{mov} of different lithofacies shale.

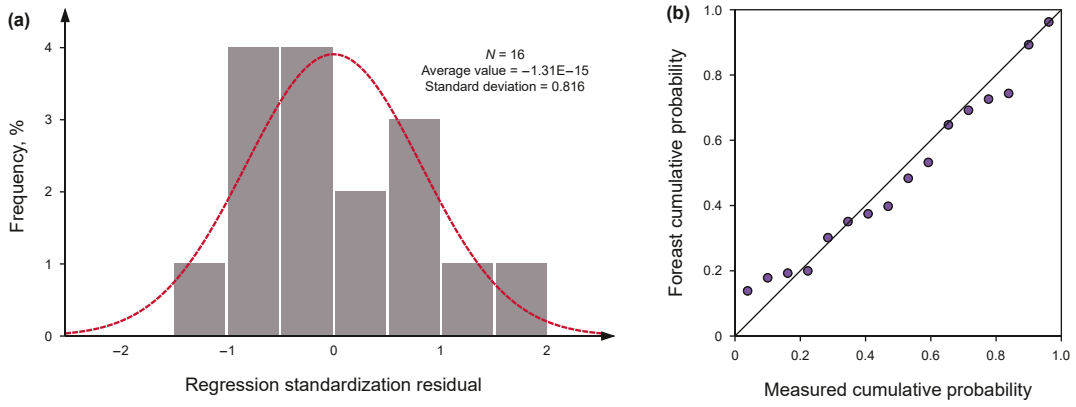

Fig. 18. Accuracy validation of the evaluation models. **(a)** Frequency histogram of regression standardized residual. **(b)** Normal P-P plot of regression standardized residual.

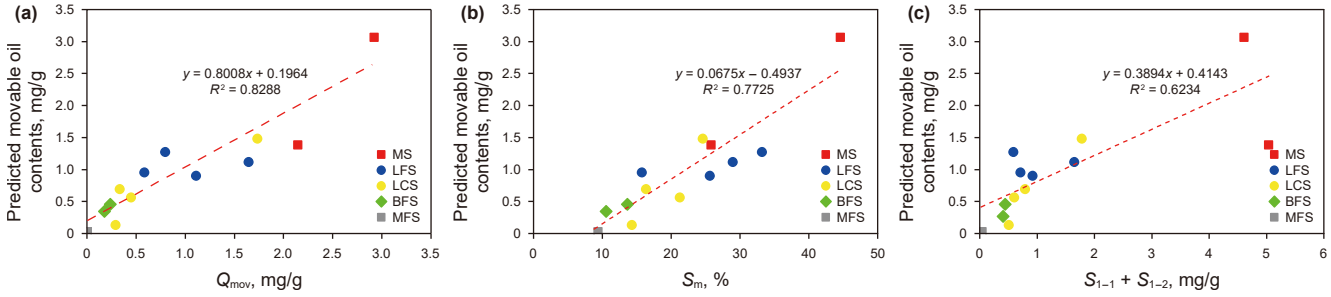

Fig. 19. Validation of the model's accuracy by comparing predicted movable oil content with main mobility evaluation parameters. **(a)** The relationship between predicted movable oil contents and Q_{mov}. **(b)** The relationship between predicted movable oil contents and S_m. **(c)** The relationship between predicted movable oil contents and $S_{1\text{-}1}$+$S_{1\text{-}2}$.

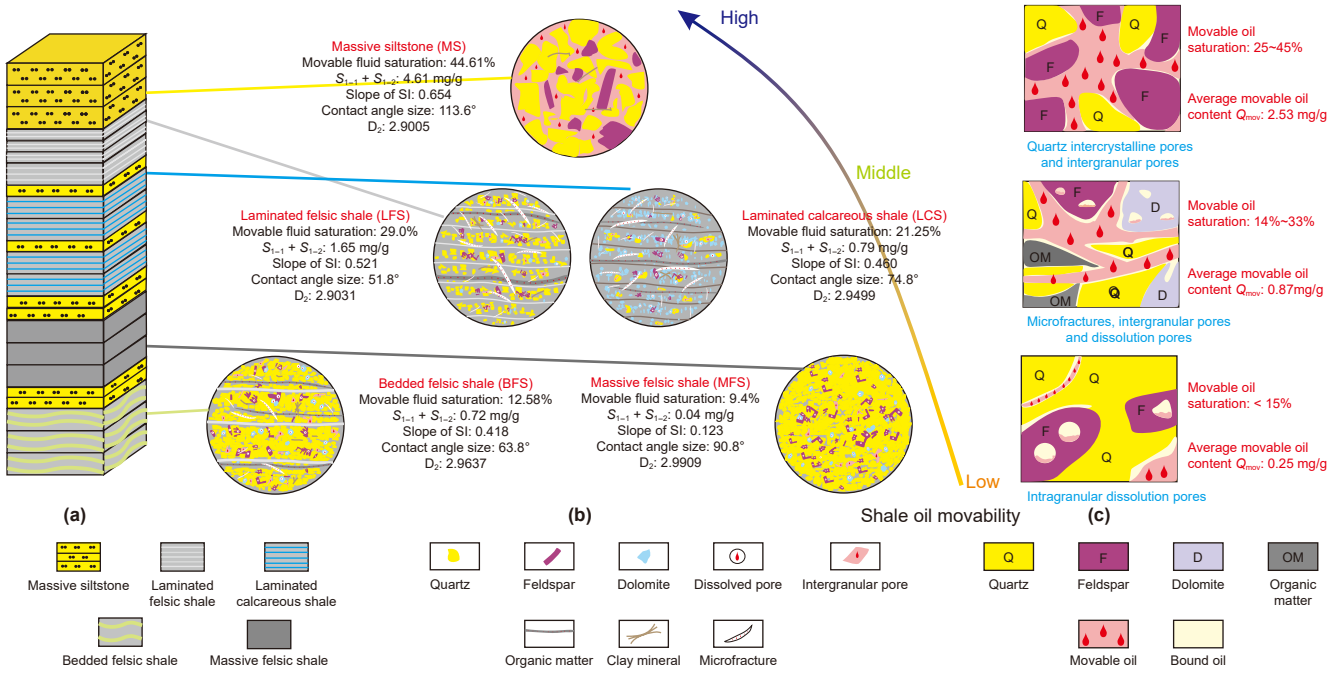

Fig. 20. Comprehensive conceptual model illustrating the variability in shale oil mobility of different lithofacies in the Fengcheng Formation of the Mahu Sag. **(a)** Different lithofacies types in Fengcheng Formation strata. **(b)** Microscopic reservoir characteristics. **(c)** Movable oil occurrence model.

connectivity, and wettability of the five lithofacies in the Fengcheng Formation shale system, elucidating the impact of reservoir properties and geochemical characteristics on shale oil mobility. Based on this, a comprehensive conceptual model was established to further explain the variations in shale oil mobility under different lithofacies controls (Fig. 20).

As shown in Fig. 20(b), MS exhibits significantly higher reservoir quality and oil-bearing potential than other lithofacies. The

MS primarily develop intergranular pores and dissolution pores associated with felsic minerals, featuring relatively large pore sizes, high SI slopes, low fractal dimensions for movable fluids (D_2), and excellent pore connectivity, forming optimal fluid flow pathways (Fig. 20(c)). This leads to the highest degree of shale oil mobility, with S_m ranging from 25% to 45%. Furthermore, as interlayers within the shale system, the MS act as reservoirs where hydrocarbons generated from adjacent organic-rich shales migrate and accumulate (Gao et al., 2024; Zhang et al., 2024b). This significant enrichment imparts strong oil-bearing potential, resulting in a high actual movable oil content (Q_{mov}) ranging from 2.1 to 2.9 mg/g. LFS and LCS exhibit moderate reservoir quality and oil-bearing potential. LFS primarily develops residual intergranular pores associated with quartz, intragranular dissolution pores linked to feldspar, and microfractures. These microfractures not only enhance fluid seepage capabilities but also connect isolated pores, maintaining relatively high SI slopes (>0.5) and low D_2 values. These microfractures are closely associated with lamination development and brittle minerals, providing effective seepage pathways for movable oil (Fig. 20(c)). The LCS also develops microfractures but predominantly features intragranular dissolution pores associated with carbonate minerals. Compared to LFS, LCS has smaller average pore sizes, weaker connectivity, and higher D_2 values, which restrict shale oil mobility. In laminated shales, bright lamination serve as better reservoir spaces where shale oil undergoes micro-migration and enrichment, resulting in moderate oil-bearing potential, with Q_{mov} ranging from 0.3 to 1.7 mg/g. BFS exhibits fewer microfractures than laminated shales, with lower SI slopes, higher D_2 values, and smaller average pore sizes, leading to reduced shale oil mobility. MFS is dense, lacking mesopores, macropores and microfractures, with the poorest pore connectivity. It exhibits the smallest average pore sizes and SI slopes and the highest D_2 values. In this lithofacies, shale oil is mainly confined in isolated micropores, resulting in poor fluid mobility. Therefore, in BFS and MFS, movable oil is mainly stored in limited microfractures and intragranular micropores (Fig. 20(c)), with S_m generally below 15% and Q_{mov} less than 0.6 mg/g.

6. Conclusions

Based on XRD mineral analysis, thin section and core observation, five lithofacies, including MS, LFS, LCS, BFS and MFS, were identified in the Fengcheng Formation shale system. Various laboratory experiments were conducted to characterize the physical properties of shale reservoirs across these lithofacies, including pore structure, connectivity, and surface wettability. Additionally, the MTP and NMR centrifugation techniques were utilized to quantitatively characterize the mobility of shale oil. MS lithofacies exhibit well-developed intergranular pores, superior pore structure and connectivity, and robust storage capacity, resulting in the highest mobility. LFS and LCS lithofacies, characterized by microfractures, intergranular pores, and intragranular dissolution pores, demonstrate moderate pore structure, connectivity, and mobility. In contrast, MFS and BFS lithofacies primarily develop intragranular dissolution pores, with more complex movable fluid pore structures and weaker connectivity, leading to lower shale oil mobility.

Shale oil mobility is controlled by multiple factors. Regarding reservoir characteristics, greater development of mesopores and macropores, higher SI slopes, and smaller D_2 values enhance reservoir properties, facilitating fluid seepage and resulting in higher S_m. Shale samples with a hydrophilic tendency also exhibit higher movable oil saturation. Geochemically, TOC content exerts a dual influence on movable oil content. Below the threshold, movable oil content increases with rising TOC levels. Additionally, shale laminations contribute to superior reservoir properties and light oil enrichment, promoting shale oil mobility.

A novel evaluation method for shale oil mobility was proposed, integrating total oil content and movable oil saturation. This approach effectively overcomes the limitations of MTP, which fails to account for the impact of pore structure on mobility. The calculated Q_{mov} values using this method showed excellent consistency with results from MTP and NMR-centrifugation experiments, providing a more accurate assessment of movable oil content in actual pore spaces.

Drawing on the lithofacies, shale reservoir characteristics, and movable oil flow space in the in the study area, a conceptual model was established to evaluate shale oil mobility variations among different lithofacies. This model aims to provide a theoretical foundation for identifying and evaluating “sweet spots” in complex shale oil reservoirs in the Fengcheng Formation of the Mahu Sag.

CRediT authorship contribution statement

Yuan-Hao Zhang: Writing – original draft, Visualization, Validation, Methodology, Investigation. **Zhen-Xue Jiang:** Supervision, Project administration, Investigation, Funding acquisition. **Jia-Qi Chang:** Writing – original draft, Methodology, Data curation. **Zhi-Ye Gao:** Validation, Supervision, Investigation, Funding acquisition, Data curation. **Bo-Lin Zhang:** Visualization. **Zhi-Wei Wang:** Methodology. **Xiao-Xue Liu:** Methodology. **Li-Liang Huang:** Resources, Project administration.

Data availability

Data will be made available on request.

Declaration of competing interest

The authors declare that they have no known competing financial interests or personal relationships that could have appeared to influence the work reported in this paper.

Acknowledgments

This work is financially supported by National Natural Science Foundation of China (42272137 and U24A20592), the Strategic Cooperation Technology Projecti of CNPC and CUPB (ZLZX2020-01-05), and AAPG Foundation Grants-in-Aid.

References

Afekare, D., Garno, J., Rao, D., 2021. Enhancing oil recovery using silica nanoparticles: nanoscale wettability alteration effects and implications for shale oil recovery. J. Petrol. Sci. Eng. 203, 108897. https://doi.org/10.1016/j.petrol.2021.108897.

Almudhhi, S., Alostath, M., Al-Bazzaz, W., Sharifigaliuk, H., Qubian, A., 2022. An unconventional approach in investigating wettability contact angle measurement in shale resources. Petrol. Sci. Technol. 40 (8), 893–936. https://doi.org/10.1080/10916466.2021.2008969.

Aman e Room, S., Zhonghong, C., Ullah, H., Ahmad, W., Ali, M., 2023. Reservoir characteristics and controlling factors of Permian glutenite in Northern Zhongghai uplift, Junggar Basin, China. Ore Energy Res. Geol. 15, 100025. https://doi.org/10.1016/j.oreoa.2023.100025.

Arthur, M.A., Cole, D.R., 2014. Unconventional hydrocarbon resources: Prospects and problems. Elements 10 (4), 257–264. https://doi.org/10.2113/gselements.10.4.257.

Bai, L., Liu, B., Du, Y., Wang, B., Tian, S., Wang, L., Xue, Z., 2022. Distribution characteristics and oil mobility thresholds in lacustrine shale reservoir: Insights from N_2 adsorption experiments on samples prior to and following hydrocarbon extraction. Pet. Sci. 19 (2), 486–497. https://doi.org/10.1016/j.petsci.2021.10.018.

Bai, L., Liu, B., Fu, X., Hu, Q., Huo, Q., Wang, L., Wang, Q., Fu, L., Ostadhassan, M., 2023. A new method for evaluating the oil mobility based on the relationship

between pore structure and state of oil. Geosci. Front. 14 (6), 101684. https://doi.org/10.1016/j.gsf.2023.101684.
Bruce, C.H., 1984. Smectite dehydration—Its relation to structural development and hydrocarbon accumulation in Northern Gulf of Mexico Basin1. AAPG Bull. 68 (6), 673–683. https://doi.org/10.1306/ad461363-16f7-11d7-8645000102c1865d.
Cai, J., Jiao, X., Wang, H., He, W., Xia, Y., 2024. Multiphase fluid-rock interactions and flow behaviors in shale nanopores: a comprehensive review. Earth Sci. Rev. 257, 104884. https://doi.org/10.1016/j.earscirev.2024.104884.
Cao, J., Xia, L., Wang, T., Zhi, D., Tang, Y., Li, W., 2020. An alkaline lake in the late paleozoic ice age (LPIA): A review and new insights into paleoenvironment and petroleum geology. Earth Sci. Rev. 202, 103091. https://doi.org/10.1016/j.earscirev.2020.103091.
Cao, Y., Jin, Z., Zhu, R., Liu, K., Bai, J., 2024a. Comprehensive evaluation of the organic-rich saline lacustrine shale in the Lucaogou Formation, Jimusar Sag, Junggar Basin, NW China. Energy 294, 130786. https://doi.org/10.1016/j.energy.2024.130786.
Cao, Y., Jin, Z.J., Zhu, R.K., Liu, K.Q., 2024b. Pore systems and their correlation with oil enrichment in various lithofacies of saline lacustrine shale strata. Int. J. Coal Geol. 282, 104444. https://doi.org/10.1016/j.coal.2024.104444.
Chandra, D., Vishal, V., Bahadur, J., Agrawal, A.K., Das, A., Hazra, B., Sen, D., 2022. Nano-scale physicochemical attributes and their impact on pore heterogeneity in shale. Fuel 314, 123070. https://doi.org/10.1016/j.fuel.2021.123070.
Chang, J., Jiang, Z., Gao, Z., Zheng, G., Zhang, Y., Huang, L., He, W., Duan, L., Chen, Z., Song, J., 2022. Oil bearing and mobility characteristics of different lithofacies shales in Fengcheng formation, Mahu Sag. J. Centr. South Univ. Sci. Technol. 53 (9), 3354–3367. https://doi.org/10.11817/j.issn.1672-7207.2022.09.007 (in Chinese).
Chang, J.Q., Jiang, Z.X., Jin, Z.H., Gao, Z.Y., Zhang, Y.H., Chen, Z.X., Huang, L.L., He, W.J., Wan, C.X., Qiu, H.Y., Xue, Z.X., 2024. Complementary laboratory experiments and molecular dynamics simulation method to investigate the mobility of shale oil: The Permian Fengcheng Formation in the Mahu Sag, Junggar Basin. Mar. Petrol. Geol. 167, 106974. https://doi.org/10.1016/j.marpetgeo.2024.106974.
Chauve, T., Scholtès, L., Donzé, F.V., Mondol, N.H., Renard, F., 2020. Layering in shales controls microfracturing at the onset of primary migration in source rocks. J. Geophys. Res. Solid Earth 125 (5), e2020JB019444. https://doi.org/10.1029/2020jb019444.
Curiale, J.A., Curtis, J.B., 2016. Organic geochemical applications to the exploration for source-rock reservoirs – a review. J. Unconvent. Oil Gas Res. 13, 1–31. https://doi.org/10.1016/j.juogr.2015.10.001.
Daigle, H., Johnson, A., 2016. Combining mercury intrusion and nuclear magnetic resonance measurements using percolation theory. Transp. Porous Media 111, 669–679. https://doi.org/10.1007/s11242-015-0619-1.
Du, X., Jin, Z., Zeng, L., Liu, G., He, W., Ostadhassan, M., Song, Y., Liang, X., Yang, S., Lu, G., 2023. Formation of natural fractures and their impact on shale oil accumulation in the Mahu Sag, Junggar Basin, NW China. Int. J. Coal Geol. 279, 104385. https://doi.org/10.1016/j.coal.2023.104385.
Fu, J., Li, S., Niu, X., Deng, X., Zhou, X., 2020. Geological characteristics and exploration of shale oil in Chang 7 Member of Triassic Yanchang Formation, Ordos Basin, NW China. Petrol. Explor. Dev. 47 (5), 870–883. https://doi.org/10.1016/S1876-3804(20)60107-0.
Gao, F., Song, Y., Li, Z., Xiong, F., Chen, L., Zhang, Y., Liang, Z., Zhang, X., Chen, Z., Joachim, M., 2018a. Lithofacies and reservoir characteristics of the Lower Cretaceous continental Shahezi Shale in the Changling fault depression of Songliao Basin, NE China. Mar. Petrol. Geol. 98, 401–421. https://doi.org/10.1016/j.marpetgeo.2018.08.035.
Gao, Z., Bai, L., Hu, Q., Yang, Z., Jiang, Z., Wang, Z., Xin, H., Zhang, L., Yang, A., Jia, L., Liu, Z., Ma, G., 2024. Shale oil migration across multiple scales: A review of characterization methods and different patterns. Earth Sci. Rev. 254, 104819. https://doi.org/10.1016/j.earscirev.2024.104819.
Gao, Z.Y., Duan, L.F., Jiang, Z.X., Huang, L.L., Chang, J.Q., Zheng, G.W., Wang, Z.W., An, F., Wei, W.H., 2023. Using laser scanning confocal microscopy combined with saturated oil experiment to investigate the pseudo in-situ occurrence mechanism of light and heavy components of shale oil in sub-micron scale. Geoenergy Sci. Eng. 220, 111234. https://doi.org/10.1016/j.petrol.2022.111234.
Gao, Z.Y., Hu, Q.H., 2016. Wettability of Mississippian Barnett Shale samples at different depths: Investigations from directional spontaneous imbibition. AAPG Bull. 100 (1), 101–114. https://doi.org/10.1306/09141514095.
Gao, Z.Y., Yang, S., Jiang, Z.X., Zhang, K., Chen, L., 2018b. Investigating the spontaneous imbibition characteristics of continental Jurassic Ziliujing Formation shale from the northeastern Sichuan Basin and correlations to pore structure and composition. Mar. Petrol. Geol. 98, 697–705. https://doi.org/10.1016/j.marpetgeo.2018.09.023.
Geistlinger, H., Mohammadian, S., 2015. Capillary trapping mechanism in strongly water wet systems: comparison between experiment and percolation theory. Adv. Water Resour. 79, 35–50. https://doi.org/10.1016/j.advwatres.2015.02.010.
Gong, D.Y., Bai, L.X., Gao, Z.Y., Qin, Z.J., Wang, Z.W., Wei, W.H., Yang, A.D., Wang, R.J., 2023. Occurrence mechanisms of laminated-type and sandwich-type shale oil in the Fengcheng Formation of Mahu Sag, Junggar Basin. Energy Fuels 37 (18), 13960–13975. https://doi.org/10.1021/acs.energyfuels.3c02625.
Gong, H.J., Jiang, Z.X., Gao, Z.Y., Zhang, F., Li, T.W., Su, S.Y., Yang, Z.W., Xiao, Y., Men, K., 2021. Innovative standard for graded evaluation of oil enrichment of lacustrine shale: A case study of the lower third member of the Shahejie Formation, Zhanhua Sag, Eastern China. Energy Fuels 35 (21), 17698–17710. https://doi.org/10.1021/acs.energyfuels.1c03014.
Guo, P., Wen, H.G., Gibert, L., Jin, J., Jiang, Y.Q., Wang, G.Z., 2021. Controlling factors of high-quality hydrocarbon source rocks developed in lacustrine shallow-water zone of the Junggar Basin, Northwestern China. AAPG Bull. 105 (10), 2063–2092. https://doi.org/10.1306/03122119013.
Han, W., Zhao, X., Jin, F., Pu, X., Chen, S., Mu, L., Zhang, W., Shi, Z., Wang, H., 2021. Sweet spots evaluation and exploration of lacustrine shale oil of the second member of Paleogene Kongdian Formation in Cangdong Sag, Bohai Bay Basin. Petrol. Explor. Dev. 48 (4), 777–786. https://doi.org/10.1016/S1876-3804(21)60075-7.
He, W., Sun, Z., Qian, M., Yang, Z., Li, Z., Leng, J., Wan, M., 2022. Evaluation of the oil-bearing properties of shale and shale oil mobility in the Fengcheng Formation in the Mahu Sag, Junggar Basin, Northwest China: A case study of well Maye-1. Geofluids 2022 (1), 6206645. https://doi.org/10.1155/2022/6206645.
He, X., Luo, Q., Jiang, Z., Qiu, Z., Luo, J., Li, Y., Deng, Y., 2024. Control of complex lithofacies on the shale oil potential in saline lacustrine basins of the Jimsar Sag, NW China: Coupling mechanisms and conceptual models. J. Asian Earth Sci. 266, 106135. https://doi.org/10.1016/j.jseaes.2024.106135.
Hu, Q., Liu, H., Li, M., Li, Z., Yang, R., Zhang, Y., Sun, M., 2018. Wettability, pore connectivity and fluid-tracer migration in shale oil reservoirs of Paleogene Shahejie Formation in Dongying sag of Bohai Bay Basin, East China. Acta Pet. Sin. 39 (3), 278–289.
Hu, S.Y., Zhao, W.Z., Hou, L.H., Yang, Z., Zhu, R.K., Wu, S.T., Bai, B., Jin, X., 2020. Development potential and technical strategy of continental shale oil in China. Petrol. Explor. Dev. 47 (4), 877–887. https://doi.org/10.1016/s1876-3804(20)60103-3.
Hu, T., Liu, Y., Jiang, F., Pang, X., Wang, Q., Zhou, K., Wu, G., Jiang, Z., Huang, L., Jiang, S., Zhang, C., Li, M., Chen, Z., 2024. A novel method for quantifying hydrocarbon micromigration in heterogeneous shale and the controlling mechanism. Energy 288, 129712. https://doi.org/10.1016/j.energy.2023.129712.
Hu, T., Pang, X., Jiang, F., Wang, Q., Liu, X., Wang, Z., Jiang, S., Wu, G., Li, C., Xu, T., Li, M., Yu, J., Zhang, C., 2021. Movable oil content evaluation of lacustrine organic-rich shales: Methods and a novel quantitative evaluation model. Earth Sci. Rev. 214, 103545. https://doi.org/10.1016/j.earscirev.2021.103545.
Huang, Y., Wang, G., Song, L., Wang, S., Zhang, Y., Huang, L., Lai, J., 2022. Fracture logging identification and effectiveness analysis of shale reservoir of the Permian Fengcheng Formation in Mahu sag, Junggar Basin. J. Palaeogeogr. 24 (3), 540–555. https://doi.org/10.7605/gdlxb.2022.03.031.
Huang, Y., Wang, G., Zhang, Y., Xi, J., Huang, L., Wang, S., Zhang, Y., Lai, J., Jiang, C., 2023. Logging evaluation of pore structure and reservoir quality in shale oil reservoir: The Fengcheng Formation in Mahu Sag, Junggar Basin, China. Mar. Petrol. Geol. 156, 106454. https://doi.org/10.1016/j.marpetgeo.2023.106454.
Jarvie, D.M., 2012. Shale resource systems for oil and gas: Part 2—Shale-oil resource systems. AAPG Memoir 97 (4), 89–119. https://doi.org/10.1306/13321447M973489.
Jia, L., Yang, Z., Gao, Z., Ma, G., Fan, Y., Hou, M., Liu, Z., 2024. The occurrence characteristics and enrichment patterns of shale oil in different lithofacies: A case study of the fengcheng formation in the mahu sag. ACS Omega 9 (46), 46505–46518. https://doi.org/10.1021/acsomega.4c08075.
Jiang, F., Hu, M., Hu, T., Lyu, J., Huang, L., Liu, C., Jiang, Z., Huang, R., Zhang, C., Wu, G., Wu, Y., 2023. Controlling factors and models of shale oil enrichment in Lower Permian Fengcheng Formation, Mahu Sag, Junggar Basin, NW China. Petrol. Explor. Dev. 50 (4), 812–825. https://doi.org/10.1016/s1876-3804(23)60430-6.
Jiang, Q., Li, M., Qian, M., Li, Z., Li, Z., Huang, Z., Zhang, C., Ma, Y., 2016. Quantitative characterization of shale oil in different occurrence states and its application. Petrol. Geol. Exp. 38 (6), 842–849. https://doi.org/10.11781/sysydz201606842.
Jiang, Z., Li, T., Gong, H., Jiang, T., Chang, J., Ning, C., Su, S., Chen, W., 2020. Characteristics of low-mature shale reservoirs in Zhanhua sag and their influence on the mobility of shale oil. Acta Pet. Sin. 41 (12), 1587–1600. https://doi.org/10.7623/syxb202012011 (in Chinese).
Jin, X., Li, G., Meng, S., Wang, X., Liu, C., Tao, J., Liu, H., 2021a. Microscale comprehensive evaluation of continental shale oil recoverability. Petrol. Explor. Dev. 48 (1), 256–268. https://doi.org/10.1016/s1876-3804(21)60021-6.
Jin, Z.J., Zhu, R.K., Liang, X.P., Shen, Y.Q., 2021b. Several issues worthy of attention in current lacustrine shale oil exploration and development. Petrol. Explor. Dev. 48 (6), 1471–1484. https://doi.org/10.1016/s1876-3804(21)60303-8.
Karimi, S., Saidian, M., Prasad, M., Kazemi, H., 2015. Reservoir rock characterization using centrifuge and nuclear magnetic resonance: A laboratory study of middle Bakken cores. In: SPE Annual Technical Conference and Exhibition. https://doi.org/10.2118/175069-MS.
Lan, Q., Xu, M., Binazadeh, M., Dehghanpour, H., Wood, J.M., 2015. A comparative investigation of shale wettability: the significance of pore connectivity. J. Nat. Gas Sci. Eng. 27, 1174–1188. https://doi.org/10.1016/j.jngse.2015.09.064.
Li, J., Jiang, C., Wang, M., Lu, S., Chen, Z., Chen, G., Li, J., Li, Z., Lu, S., 2020. Adsorbed and free hydrocarbons in unconventional shale reservoir: a new insight from NMR T_1-T_2 maps. Mar. Petrol. Geol. 116 (2), 104311. https://doi.org/10.1016/j.marpetgeo.2020.104311.
Li, J., Lu, S., Cai, J., Zhang, P., Xue, H., Zhao, X., 2018a. Adsorbed and free oil in lacustrine nanoporous shale: a theoretical model and a case study. Energy Fuels 32 (12), 12247–12258. https://doi.org/10.1021/acs.energyfuels.8b02953.
Li, J., Lu, S., Jiang, C., Wang, M., Chen, Z., Chen, G., Li, J., Lu, S., 2019a. Characterization of shale pore size distribution by NMR considering the influence of

shale skeleton signals. Energy Fuels 33 (7), 6361–6372. https://doi.org/10.1021/acs.energyfuels.9b01317.
Li, J., Wang, S., Lu, S., Zhang, P., Cai, J., Zhao, J., Li, W., 2019b. Microdistribution and mobility of water in gas shale: A theoretical and experimental study. Mar. Petrol. Geol. 102, 496–507. https://doi.org/10.1016/j.marpetgeo.2019.01.012.
Li, J., You, H., Zhang, X., Zhao, S., Jiang, F., Feng, G., Su, Y., Zhang, Y., Xue, J., 2024a. Influence of shale reservoir properties on shale oil mobility and its mechanism. Energy Geosci. 5 (4), 100329. https://doi.org/10.1016/j.engeos.2024.100329.
Li, L., Huang, Z., Duan, X., Niu, H., Zhan, S., Yang, Z., Fan, Z., Zhang, T., 2024b. Insights into enhancing shale oil recovery postfracturing with CO_2 Huff and puff and elastic depletion development strategies. Energy Fuels 38 (5), 3997–4009. https://doi.org/10.1021/acs.energyfuels.3c04549.
Li, M., Chen, Z., Ma, X., Cao, T., Qian, M., Jiang, Q., Tao, G., Li, Z., Song, G., 2019c. Shale oil resource potential and oil mobility characteristics of the Eocene-Oligocene Shahejie Formation, Jiyang Super-depression, Bohai Bay Basin of China. Int. J. Coal Geol. 204, 130–143. https://doi.org/10.1016/j.coal.2019.01.013.
Li, W., Cao, J., Zhi, D., Tang, Y., He, W., Wang, T., Xia, L., 2021. Controls on shale oil accumulation in alkaline lacustrine settings: Late Paleozoic Fengcheng Formation, northwestern Junggar Basin. Mar. Petrol. Geol. 129, 105107. https://doi.org/10.1016/j.marpetgeo.2021.105107.
Li, X., Cai, J., Zhu, X., Liu, H., Li, Z., Liu, Y., 2024c. Indicative significance of the interfacial interactions between pore surface and soluble organic matter on the shale oil mobility. Colloids Surf. A Physicochem. Eng. Asp. 696, 134282. https://doi.org/10.1016/j.colsurfa.2024.134282.
Li, Z.Q., Shen, X., Qi, Z.Y., Hu, R.L., 2018b. Study on the pore structure and fractal characteristics of marine and continental shale based on mercury porosimetry, N_2 adsorption and NMR methods. J. Nat. Gas Sci. Eng. 53, 12–21. https://doi.org/10.1016/j.jngse.2018.02.027.
Lin, Z., Hu, Q., Yin, N., Yang, S., Liu, H., Chao, J., 2024. Nanopores-to-microfractures flow mechanism and remaining distribution of shale oil during dynamic water spontaneous imbibition studied by NMR. Geoenergy Sci. Eng. 241, 213202. https://doi.org/10.1016/j.geoen.2024.213202.
Liu, B., Sun, J.H., Zhang, Y.Q., He, J.L., Fu, X.F., Yang, L., Xing, J.L., Zhao, X.Q., 2021. Reservoir space and enrichment model of shale oil in the first member of Cretaceous Qingshankou Formation in the Changling Sag, southern Songliao Basin, NE China. Petrol. Explor. Dev. 48 (3), 608–624. https://doi.org/10.1016/s1876-3804(21)60049-6.
Liu, H.M., Zhang, S., Song, G.Q., Zhang, S.P., Hao, X.F., Xie, Z.H., Xu, N.N., Liu, P., 2017. A discussion on the origin of shale reservoir inter-laminar fractures in the Shahejie Formation of Paleogene, Dongying Depression. J. Earth Sci. 28 (6), 1064–1077. https://doi.org/10.1007/s12583-016-0946-3.
Liu, K., Jin, Z., Zeng, L., Wang, Z., Ostadhassan, M., Wang, Y., Liang, X., Cao, Y., Liu, G., 2023. Enrichment of free oil in alkaline lacustrine Fengcheng Formation in Mahu Sag. Geoenergy Sci. Eng. 228, 212015. https://doi.org/10.1016/j.geoen.2023.212015.
Liu, Y., Yao, Y., Liu, D., Zheng, S., Sun, G., Chang, Y., 2018. Shale pore size classification: an NMR fluid typing method. Mar. Petrol. Geol. 96, 591–601. https://doi.org/10.1016/j.marpetgeo.2018.05.014.
Ma, X., Guo, S.B., Shi, D.S., Zhou, Z., Liu, G.H., 2019. Investigation of pore structure and fractal characteristics of marine-continental transitional shales from Longtan Formation using MICP, gas adsorption, and NMR (Guizhou, China). Mar. Petrol. Geol. 107, 555–571. https://doi.org/10.1016/j.marpetgeo.2019.05.018.
McMahon, T.P., Larson, T.E., Zhang, T., Shuster, M., 2024. Geologic characteristics,exploration and production progress of shale oil and gas in the United states:an overview. Petrol. Explor. Dev. 51 (4), 807–828. https://doi.org/10.1016/S1876-3804(24)60516-1.
Meng, Q.F., Hao, F., Tian, J.Q., 2021. Origins of non-tectonic fractures in shale. Earth Sci. Rev. 222, 13. https://doi.org/10.1016/j.earscirev.2021.103825.
Mitchell, J., Chandrasekera, T.C., Johns, M.L., Gladden, L.F., Fordham, E.J., 2010. Nuclear magnetic resonance relaxation and diffusion in the presence of internal gradients: The effect of magnetic field strength. Phys. Rev. 81 (2), 026101. https://doi.org/10.1103/PhysRevE.81.026101.
Nie, S., Yang, F., Luo, L., Deng, K., Du, L., 2024. Experimental investigation on the oil occurrence and mobility of lacustrine shales in offshore area of China using 1D/2D nuclear magnetic resonance and centrifugal techniques. Int. J. Coal Geol. 294, 104618. https://doi.org/10.1016/j.coal.2024.104618.
Oboh-Ikuenobe, F.E., Obi, C.G., Jaramillo, C.A., 2005. Lithofacies, palynofacies, and sequence stratigraphy of Palaeogene strata in Southeastern Nigeria. J. Afr. Earth Sci. 41 (1), 79–101. https://doi.org/10.1016/j.jafrearsci.2005.02.002.
Ougier-Simonin, A., Renard, F., Boehm, C., Vidal-Gilbert, S., 2016. Microfracturing and microporosity in shales. Earth Sci. Rev. 162, 198–226. https://doi.org/10.1016/j.earscirev.2016.09.006.
Pang, X., Li, M., Li, B., Wang, T., Hui, S., Liu, Y., Liu, G., Hu, T., Xu, T., Jiang, F., Pang, H., Wang, C., 2023. Main controlling factors and movability evaluation of continental shale oil. Earth Sci. Rev. 243, 104472. https://doi.org/10.1016/j.earscirev.2023.104472.
Pang, X., Wang, G., Kuang, L., Li, H., Zhao, Y., Li, D., Zhao, X., Wu, S., Feng, Z., Lai, J., 2022. Insights into the pore structure and oil mobility in fine-grained sedimentary rocks: The Lucaogou Formation in Jimusar Sag, Junggar Basin, China. Mar. Petrol. Geol. 137, 105492. https://doi.org/10.1016/j.marpetgeo.2021.105492.
Pfeifer, P., Avnir, D., 1984. Chemistry in noninteger dimensions between two and three. I. Fractal theory of heterogeneous surfaces. J. Chem. Phys. 80 (7), 3558–3565. https://doi.org/10.1063/1.447307.
Piedrahita, J., Aguilera, R., 2017. Estimating oil saturation index OSI from NMR logging and comparison with Rock-Eval pyrolysis measurements in a shale oil reservoir. In: SPE Unconventional Resources Conference. https://doi.org/10.2118/185073-MS.
Princeton Dim, C.I., Okwara, I.C., Mode, A.W., Onuoha, K.M., 2016. Lithofacies and environments of deposition within the middle–upper Cretaceous successions of Southeastern Nigeria. Arabian J. Geosci. 9 (6), 447. https://doi.org/10.1007/s12517-016-2486-7.
Rahman, H.M., Kennedy, M., Löhr, S., Dewhurst, D.N., 2017. Clay-organic association as a control on hydrocarbon generation in shale. Org. Geochem. 105, 42–55. https://doi.org/10.1016/j.orggeochem.2017.01.011.
Ram, F., Bera, M.K., Sarkar, A., 2022. An optimized accelerated solvent extraction and purification method for enhanced recovery of *n*-alkanes (notably short-chains) from environmental samples using the conventional dichloromethane/methanol solvent. Org. Geochem. 165, 104368. https://doi.org/10.1016/j.orggeochem.2022.104368.
Ravikovitch, P.I., Neimark, A.V., 2002. Experimental confirmation of different mechanisms of evaporation from ink-bottle type pores: Equilibrium, pore blocking, and cavitation. Langmuir 18 (25), 9830–9837. https://doi.org/10.1021/la026140z.
Saidian, M., Prasad, M., 2015. Effect of mineralogy on nuclear magnetic resonance surface relaxivity: A case study of middle Bakken and three forks formations. Fuel 161, 197–206. https://doi.org/10.1016/j.fuel.2015.08.014.
Salmon, V., Derenne, S., Lallier-Vergés, E., Largeau, C., Beaudoin, B., 2000. Protection of organic matter by mineral matrix in a Cenomanian black shale. Org. Geochem. 31 (5), 463–474. https://doi.org/10.1016/s0146-6380(00)00013-9.
Shi, K.Y., Chen, J.Q., Pang, X.Q., Jiang, F.J., Hui, S.S., Pang, H., Ma, K.Y., Cong, Q., 2022. Effect of wettability of shale on CO_2 sequestration with enhanced gas recovery in shale reservoir: Implications from molecular dynamics simulation. J. Nat. Gas Sci. Eng. 107, 104798. https://doi.org/10.1016/j.jngse.2022.104798.
Shu, Y., Bao, H.Y., Zheng, Y.H., Chen, M.K., Lu, Y.C., Liu, H.T., Peng, W., Zhou, L., Ma, Y.Q., Wen, Y.R., Wang, Q.M., Zhang, Z.Y., 2021. Lithofacies types, assemblage characteristics, and sedimentary evolution model of lacustrine shale in Dongyuemiao Formation of Fuxing area. Front. Earth Sci. 9, 772581. https://doi.org/10.3389/feart.2021.772581.
Slatt, R.M., 2011. Important geological properties of unconventional resource shales. Cent. Eur. J. Geosci. 3 (4), 435–448. https://doi.org/10.2478/s13533-011-0042-2.
Song, Z.Z., Zhang, J., Jin, S.G., Liu, C.Q., Abula, A., Hou, J.K., Ma, L., 2024. The occurrences and mobility of shale oil in the pore space of terrestrial shale. Fuel 374, 132377. https://doi.org/10.1016/j.fuel.2024.132377.
Sun, B., Liu, X.P., Zhao, X.Z., Gingras, M., Jin, F.M., Liu, T., Hua, Z.X., Peng, W.D., Yuan, Y., 2025. Laminated shale oil system mobility and controlling factors of the Paleogene Shahejie Formation: Evidences from T_1-T_2 NMR experiments, multi-temperature pyrolysis and confocal laser scanning microscopy. Fuel 379, 133015. https://doi.org/10.1016/j.fuel.2024.133015.
Sun, L.D., Liu, H., He, W.Y., Li, G.X., Zhang, S.C., Zhu, R.K., Jin, X., Meng, S.W., Jiang, H., 2021. An analysis of major scientific problems and research paths of Gulong shale oil in Daqing Oilfield, NE China. Petrol. Explor. Dev. 48 (3), 527–540. https://doi.org/10.1016/s1876-3804(21)60043-5.
Sun, W.J.B., Zuo, Y.J., Wu, Z.H., Liu, H., Xi, S.J., Shui, Y., Wang, J., Liu, R.B., Lin, J.Y., 2019. Fractal analysis of pores and the pore structure of the Lower Cambrian Niutitang shale in northern Guizhou Province: Investigations using NMR, SEM and image analyses. Mar. Petrol. Geol. 99 (1), 416–428. https://doi.org/10.1016/j.marpetgeo.2018.10.042.
Tang, W.B., Zhang, Y.Y., Pe-Piper, G., Piper, D.J.W., Guo, Z.J., Li, W., 2020. Soft-sediment deformation structures in alkaline lake deposits of Lower Permian Fengcheng Formation, Junggar Basin, NW China: Implications for syn-sedimentary tectonic activity. Sediment. Geol. 406, 105719. https://doi.org/10.1016/j.sedgeo.2020.105719.
Tang, Y., Cao, J., He, W.J., Guo, X.G., Zhao, K.B., Li, W.W., 2021. Discovery of shale oil in alkaline lacustrine basins: The late Paleozoic Fengcheng Formation, Mahu Sag, Junggar Basin, China. Pet. Sci. 18 (5), 1281–1293. https://doi.org/10.1016/j.petsci.2021.04.001.
Tao, K., Cao, J., Chen, X., Nueraili, Z., Hu, W., Shi, C., 2019. Deep hydrocarbons in the northwestern Junggar basin (NW China): Geochemistry, origin, and implications for the oil vs. gas generation potential of post-mature saline lacustrine source rocks. Mar. Petrol. Geol. 109, 623–640. https://doi.org/10.1016/j.marpetgeo.2019.06.041.
Teixeira, M.G., Donzé, F., Renard, F., Panahi, H., Papachristos, E., Scholtès, L., 2017. Microfracturing during primary migration in shales. Tectonophysics 694, 268–279. https://doi.org/10.1016/j.tecto.2016.11.010.
Testamanti, M.N., Rezaee, R., 2017. Determination of NMR T_2 cut-off for clay bound water in shales: A case study of Carynginia Formation, Perth Basin, Western Australia. J. Petrol. Sci. Eng. 149, 497–503. https://doi.org/10.1016/j.petrol.2016.10.066.
Thommes, M., Kaneko, K., Neimark, A.V., Olivier, J.P., Rodriguez-Reinoso, F., Rouquerol, J., Sing, K.S., 2015. Physisorption of gases, with special reference to the evaluation of surface area and pore size distribution (IUPAC technical report). Pure Appl. Chem. 87 (9–10), 1051–1069. https://doi.org/10.1515/pac-2014-1117.
Tian, H., He, K., Huangfu, Y., Liao, F., Wang, X., Zhang, S., 2024. Oil content and mobility in a shale reservoir in Songliao Basin, Northeast China: Insights from combined solvent extraction and NMR methods. Fuel 357, 129678. https://doi.org/10.1016/j.fuel.2023.129678.

Tian, S.S., Erastova, V., Lu, S.F., Greenwell, H.C., Underwood, T.R., Xue, H.T., Zeng, F., Chen, G.H., Wu, C.Z., Zhao, R.X., 2018. Understanding model crude oil component interactions on kaolinite silicate and aluminol surfaces: Toward improved understanding of shale oil recovery. Energy Fuels 32 (2), 1155–1165. https://doi.org/10.1021/acs.energyfuels.7b02763.

Wang, M., Guo, Z.Q., Jiao, C.X., Lu, S.F., Li, J.B., Xue, H.T., Li, J.J., Li, J.Q., Chen, G.H., 2019a. Exploration progress and geochemical features of lacustrine shale oils in China. J. Petrol. Sci. Eng. 178, 975–986. https://doi.org/10.1016/j.petrol.2019.04.029.

Wang, M., Ma, R., Li, J.B., Lu, S.F., Li, C.M., Guo, Z.L., Li, Z., 2019b. Occurrence mechanism of lacustrine shale oil in the Paleogene Shahejie Formation of Jiyang Depression, Bohai Bay Basin, China. Petrol. Explor. Dev. 46 (4), 833–846. https://doi.org/10.1016/s1876-3804(19)60242-9.

Wang, S., Javadpour, F., Feng, Q., 2016. Molecular dynamics simulations of oil transport through inorganic nanopores in shale. Fuel 171, 74–86. https://doi.org/10.1016/j.fuel.2015.12.071.

Wang, S., Wang, G.W., Huang, L.L., Song, L.T., Zhang, Y.L., Li, D., Huang, Y.Y., 2021. Logging evaluation of lamina structure and reservoir quality in shale oil reservoir of Fengcheng Formation in Mahu Sag, China. Mar. Petrol. Geol. 133, 105299. https://doi.org/10.1016/j.marpetgeo.2021.105299.

Wang, X., Wang, M., Li, J., Shao, H., Deng, Z., Wu, Y., 2022. Thermal maturity: The controlling factor of wettability, pore structure, and oil content in the lacustrine Qingshankou shale, Songliao Basin. J. Petrol. Sci. Eng. 215, 110618. https://doi.org/10.1016/j.petrol.2022.110618.

Wang, Y.C., Chen, D.X., Rong, L.X., Chen, J.L., Wang, F.W., He, S.J., Wang, Y.Q., Yang, Z.J., Lei, W.Z., 2024. Evaluation of fluid mobility and factors influencing the deep tight sandstone of the third member of the Shahejie Formation in the Jiyang Depression, Bohai Bay Basin. Mar. Petrol. Geol. 170, 107090. https://doi.org/10.1016/j.marpetgeo.2024.107090.

Wang, Z., Gao, Z., He, W., Yang, L., Huang, L., Jiang, Z., Chang, J., Zheng, G., Wei, W., Duan, L., Zhang, Y., An, F., 2023. Using spontaneous imbibition to evaluate the hydrocarbon migration and accumulation potential of shale reservoirs: A case study of the Permian Fengcheng Formation in the Mahu Sag, Junggar Basin. Energy Fuels 37 (1), 360–372. https://doi.org/10.1021/acs.energyfuels.2c03897.

Washburn, K.E., Sandor, M., Cheng, Y., 2017. Evaluation of sandstone surface relaxivity using laser-induced breakdown spectroscopy. J. Magn. Reson. 275, 80–89. https://doi.org/10.1016/j.jmr.2016.12.004.

Woo, J., Lee, H.S., Ozyer, C., Rhee, C.W., 2021. Effect of lamination on shale reservoir properties: Case study of the Montney Formation, Canada. Geofluids 2021, 14. https://doi.org/10.1155/2021/8853639.

Wu, H., Wang, Y., Tan, J., Ma, X., Hu, R., Liu, W., 2024. Influences of lithofacies on fluid mobility in mixed sedimentary rocks: Insights from NMR analysis of the middle Permian Lucaogou Formation, Junggar Basin. Energy Geoscience 5 (4), 100305. https://doi.org/10.1016/j.engeos.2024.100305.

Wu, Y., Liu, C., Jiang, F., Hu, T., Lv, J., Zhang, C., Guo, X., Huang, L., Hu, M., Huang, R., Awan, R.S., Zhao, Y., 2022. Geological characteristics and shale oil potential of alkaline lacustrine source rock in Fengcheng Formation of the Mahu Sag, Junggar Basin, Western China. J. Petrol. Sci. Eng. 216, 110823. https://doi.org/10.1016/j.petrol.2022.110823.

Xia, L., Cao, J., Stüeken, E.E., Zhi, D., Wang, T., Li, W., 2020. Unsynchronized evolution of salinity and pH of a Permian alkaline lake influenced by hydrothermal fluids: A multi-proxy geochemical study. Chem. Geol. 541, 119581. https://doi.org/10.1016/j.chemgeo.2020.119581.

Xiao, D.S., Zheng, L.H., Wang, M., Wang, R., Guan, X.D., 2024. The relationship between oiliness and mobility and their controlling factors for lacustrine shale oil: A case study of Qing 1 member in Changling Sag, Songliao Basin. Fuel 376, 132738. https://doi.org/10.1016/j.fuel.2024.132738.

Xin, B.X., Zhao, X.Z., Hao, F., Jin, F.M., Pu, X.G., Han, W.Z., Xu, Q.L., Guo, P.F., Tian, J.Q., 2022. Laminae characteristics of lacustrine shales from the Paleogene Kongdian Formation in the Cangdong Sag, Bohai Bay Basin, China: Why do laminated shales have better reservoir physical properties? Int. J. Coal Geol. 260, 104056. https://doi.org/10.1016/j.coal.2022.104056.

Xu, H., Wang, F., Liu, Y., Meng, X., Liu, L., 2024. Mechanism study on the influence of wettability on CO_2 displacement of shale oil in nanopores. Fuel 376, 132695. https://doi.org/10.1016/j.fuel.2024.132695.

Yang, W., Wang, Y.H., Xie, M., Li, Y.Y., Gao, Y., Deng, Y., Xu, C.F., Qin, J.H., Peng, S.C., Yang, L.L., Yao, L.J., Hou, H.D., 2023. Effect of lithofacies on differential movable fluid behaviors of saline lacustrine fine-grained mixed sedimentary sequences in the Jimusar Sag, Junggar Basin, NW China: Forcing mechanisms and multi-scale models. Mar. Petrol. Geol. 150, 106150. https://doi.org/10.1016/j.marpetgeo.2023.106150.

Yu, K., Cao, Y., Qiu, L., Sun, P., 2019. Depositional environments in an arid, closed basin and their implications for oil and gas exploration: The lower Permian Fengcheng Formation in the Junggar Basin, China. AAPG Bull. 103 (9), 2073–2115. https://doi.org/10.1306/01301917414.

Yu, K., Cao, Y., Qiu, L., Sun, P., Jia, X., Wan, M., 2018. Geochemical characteristics and origin of sodium carbonates in a closed alkaline basin: The Lower Permian Fengcheng Formation in the Mahu Sag, northwestern Junggar Basin, China. Palaeogeogr. Palaeoclimatol. Palaeoecol. 511, 506–531. https://doi.org/10.1016/j.palaeo.2018.09.015.

Yuan, Y., Rezaee, R., 2019. Fractal analysis of the pore structure for clay bound water and potential gas storage in shales based on NMR and N_2 gas adsorption. J. Petrol. Sci. Eng. 177 (2), 756–765. https://doi.org/10.1016/j.petrol.2019.02.082.

Zang, Q., Liu, C., Awan, R.S., Yang, X., Li, G., Wu, Y., Lu, Z., Feng, D., 2022. Occurrence characteristics of the movable fluid in heterogeneous sandstone reservoir based on fractal analysis of NMR data: a case study of the Chang 7 Member of Ansai block, Ordos Basin, China. J. Petrol. Sci. Eng. 214, 110499. https://doi.org/10.1016/j.petrol.2022.110499.

Zhang, F., Jiang, Z., Sun, W., Zhang, X., Zhu, L., Li, X., Zhao, W., 2020. Effect of microscopic pore-throat heterogeneity on gas-phase percolation capacity of tight sandstone reservoirs. Energy Fuels 34 (10), 12399–12416. https://doi.org/10.1021/acs.energyfuels.0c02393.

Zhang, J., Hu, Y., 2020. Comparative evaluation of pore structure heterogeneity in low-permeability tight sandstones using different fractal models based on NMR technology: A case study of Benxi Formation in the central Ordos Basin. Energy Fuels 34 (11), 13924–13942. https://doi.org/10.1021/acs.energyfuels.0c02738.

Zhang, J., Zhu, R., Wu, S., Jiang, X., Liu, C., Cai, Y., Zhang, S., Zhang, T., 2023. Microscopic oil occurrence in high-maturity lacustrine shales: Qingshankou Formation, Gulong Sag, Songliao Basin. Pet. Sci. 20 (5), 2726–2746. https://doi.org/10.1016/j.petsci.2023.08.026.

Zhang, L., Xu, S.Z., Jin, K., Zhang, X.J., Liu, Y.L., Chen, C., Liu, R.H., Li, M., Li, J.P., 2024a. Study on the influencing factors of oil bearing and mobility of shale reservoirs in the fourth member of the Shahejie Formation in the liaohe Western depression. Energies 17 (16), 3931. https://doi.org/10.3390/en17163931.

Zhang, P.F., Lu, S.F., Li, J.Q., Chang, X.C., Lin, Z.Z., Chen, G., Li, J.J., Liu, J.Z., Tian, S.S., 2022. Evaluating microdistribution of adsorbed and free oil in a lacustrine shale using nuclear magnetic resonance: A theoretical and experimental study. J. Petrol. Sci. Eng. 212, 110208. https://doi.org/10.1016/j.petrol.2022.110208.

Zhang, P.F., Lu, S.F., Li, J.Q., Chen, C., Xue, H.T., Zhang, J., 2018a. Petrophysical characterization of oil-bearing shales by low-field nuclear magnetic resonance (NMR). Mar. Petrol. Geol. 89, 775–785. https://doi.org/10.1016/j.marpetgeo.2017.11.015.

Zhang, Y., Chang, J., Jiang, Z., Gao, Z., Zhang, C., Wang, G., Shao, X., He, W., 2024b. Visualization of dynamic micro-migration of shale oil and investigation of shale oil movability by NMRI combined oil charging/water flooding experiments: A novel approach. Mar. Petrol. Geol. 165, 106907. https://doi.org/10.1016/j.marpetgeo.2024.106907.

Zhang, Y., Jiang, Z., Chang, J., Gao, Z., Huang, L., He, W., Zhang, C., Chen, L., Fan, Q., Han, Y., Zhang, B., Chen, C., 2025. The multi-scale pore system and its implication for shale oil occurrence in alkaline lacustrine mixed sedimentary shale reservoirs: A case study from the Fengcheng Formation, Mahu Sag, Junggar Basin. J. Earth Sci. https://doi.org/10.1007/s12583-025-0297-z.

Zhang, Z., Yuan, X., Wang, M., Zhou, C., Tang, Y., Chen, X., Lin, M., Cheng, D., 2018b. Alkaline-lacustrine deposition and paleoenvironmental evolution in Permian Fengcheng Formation at the Mahu Sag, Junggar Basin, NW China. Petrol. Explor. Dev. 45 (6), 1036–1049. https://doi.org/10.1016/S1876-3804(18)30107-1.

Zhao, R., Xue, H., Lu, S., Greenwell, H.C., Xu, Y., He, T., Erastova, V., 2024. Molecular dynamics of quantitative evaluation of confined fluid behavior in nanopores media and the influencing mechanism: Pore size and pore geometry. Phys. Fluids 36 (9), 092027. https://doi.org/10.1063/5.0226864.

Zhao, R.X., Xue, H.T., Lu, S.F., Li, J.Q., Tian, S.S., wang, M., Dong, Z.T., 2022. Multi-scale pore structure characterization of lacustrine shale and its coupling relationship with material composition: an integrated study of multiple experiments. Mar. Petrol. Geol. 140 (5), 105648. https://doi.org/10.1016/j.marpetgeo.2022.105648.

Zhao, W., Zhu, R., Hu, S., Hou, L., Wu, S., 2020. Accumulation contribution differences between lacustrine organic-rich shales and mudstones and their significance in shale oil evaluation. Petrol. Explor. Dev. 47 (6), 1079–1089. https://doi.org/10.1016/S1876-3804(20)60126-X.

Zhao, X., Sang, Q., Li, Y., Shi, L., Liu, H., Dong, M., 2021. Mobilization of oil in organic matter and its contribution to oil production during primary production in shale. Fuel 287, 119449. https://doi.org/10.1016/j.fuel.2020.119449.

Zheng, S., Yao, Y., Liu, D., Sang, S., Liu, S., Wang, M., Zhou, X., Wang, R., Han, S., Liu, T., 2023. Re-evaluating the accurate multiphase water distribution in coals: Unifying experiment and theory. Chem. Eng. J. 464, 142637. https://doi.org/10.1016/j.cej.2023.142637.

Zheng, S.J., Yao, Y.B., Liu, D.M., Cai, Y.D., Liu, Y., 2019. Nuclear magnetic resonance surface relaxivity of coals. Int. J. Coal Geol. 205, 1–13. https://doi.org/10.1016/j.coal.2019.02.010.

Zhi, D., Tang, Y., He, W., Guo, X., Zheng, M., Huang, L., 2021. Orderly coexistence and accumulation models of conventional and unconventional hydrocarbons in Lower Permian Fengcheng Formation, Mahu Sag, Junggar Basin. Petrol. Explor. Dev. 48 (1), 38–51. https://doi.org/10.1016/S1876-3804(21)60004-6.

Zhi, D., Tang, Y., Zheng, M., Xu, Y., Cao, J., Ding, J., Zhao, C., 2019. Geological characteristics and accumulation controlling factors of shale reservoirs in Fengcheng Formation, Mahu Sag, Junggar Basin. China Petrol. Expl. 24 (5), 615–623. https://doi.org/10.3969/j.issn.1672-7703.2019.05.008.

Zhou, H.W., Liu, Z.L., Zhong, J.C., Chen, B.C., Zhao, J.W., Xue, D.J., 2022. NMRI online observation of coal fracture and pore structure evolution under confining pressure and axial compressive loads: A novel approach. Energy 261, 125297. https://doi.org/10.1016/j.energy.2022.125297.

Zhou, L., Kang, Z.H., 2016. Fractal characterization of pores in shales using NMR: A case study from the Lower Cambrian Niutitang Formation in the middle Yangtze platform, Southwest China. J. Nat. Gas Sci. Eng. 35 (9), 860–872. https://doi.org/10.1016/j.jngse.2016.09.030.

Zhu, C., Guo, W., Li, Y., Gong, H., Sheng, J.J., Dong, M., 2021. Effect of occurrence states of fluid and pore structures on shale oil movability. Fuel 288, 119847. https://doi.org/10.1016/j.fuel.2020.119847.

Zhu, X., Zhang, S., Cai, J., Liu, H., Li, Z., 2024. Occurrence and mobility of shale oil in the Jiyang Depression, Eastern China. J. Asian Earth Sci. 270, 106187. https://doi.org/10.1016/j.jseaes.2024.106187.

Zou, C.N., Zhu, R.K., Chen, Z.Q., Ogg, J.G., Wu, S.T., Dong, D.Z., Qiu, Z., Wang, Y.M., Wang, L., Lin, S.H., Cui, J.W., Su, L., Yang, Z., 2019. Organic-matter-rich shales of China. Earth Sci. Rev. 189, 51–78. https://doi.org/10.1016/j.earscirev.2018.12.002.